

Effects of cloud-radiative heating on atmospheric general circulation model (AGCM) simulations of convectively coupled equatorial waves

Jia-Lin Lin,^{1,2} Daehyun Kim,³ Myong-In Lee,⁴ and In-Sik Kang³

Received 28 November 2006; revised 14 July 2007; accepted 22 August 2007; published 27 December 2007.

[1] This study examines the effects of cloud-radiative heating on convectively coupled equatorial waves simulated by the Seoul National University (SNU) atmospheric general circulation model (AGCM). The strength of cloud-radiative heating is adjusted by modifying the autoconversion rate needed for cloud condensates to grow up to raindrops. The results show that increasing the autoconversion rate has little effect on the climatological mean precipitation, but it significantly reduces the time-mean clouds and radiative heating in the upper troposphere and enhances heating due to moist processes in the middle troposphere. These lead to cooling of time-mean upper troposphere temperature and drying of lower-troposphere moisture. Reduction of cloud-radiative heating enhances the prominence of Kelvin and $n = 0$ eastward inertial gravity (EIG) waves. It also tends to enhance significantly the variance of the Kelvin, equatorial Rossby (ER), mixed Rossby-gravity (MRG), and $n = 1$ westward inertial gravity (WIG) waves, but not the Madden-Julian Oscillation (MJO) or $n = 0$ EIG wave. Reduction of cloud-radiative heating has little effect on the phase speed of the waves, which is associated with unchanged effective static stability caused by the near cancellation between reduced dry static stability and reduced diabatic heating. An important implication of this study is that when tuning GCM's top-of-the-atmosphere radiative fluxes to fit the observations, one needs to make sure that the enhancement factor of cloud-radiative heating at the intraseasonal timescale also fits with the observation so that the convectively coupled equatorial waves are not suppressed.

Citation: Lin, J.-L., D. Kim, M.-I. Lee, and I.-S. Kang (2007), Effects of cloud-radiative heating on atmospheric general circulation model (AGCM) simulations of convectively coupled equatorial waves, *J. Geophys. Res.*, 112, D24107, doi:10.1029/2006JD008291.

1. Introduction

[2] The tropical deep convection does not occur randomly, but is often organized by convectively coupled equatorial waves, such as the Madden-Julian Oscillation [Madden and Julian, 1971], Kelvin, equatorial Rossby (ER), mixed Rossby-gravity (MRG), and eastward inertio-gravity (EIG) and westward inertio-gravity (WIG) waves [e.g., Takayabu, 1994; Wheeler and Kiladis, 1999; hereinafter, WK]. These waves significantly affect a wide range of tropical weather such as the onset and breaks of the Indian and Australian summer monsoons [e.g., Yasunari, 1979; Wheeler and McBride, 2005] and the formation of tropical cyclones in almost all basins [e.g., Liebmann et al., 1994; Maloney and Hartmann, 2001; Bessafi and Wheeler, 2005]. On a

longer timescale the convectively coupled equatorial waves also trigger or terminate some El Niño events [e.g., Kessler et al., 1995; Takayabu et al., 1999; Bergman et al., 2001; Roundy and Kiladis, 2006]. Therefore these waves are important for both weather prediction and climate prediction.

[3] Unfortunately, these convectively coupled equatorial waves are not well simulated in the general circulation models (GCMs) used for predictions and projections. For example, poor simulation of the Madden-Julian Oscillation (MJO) has been a well-known long-standing problem in GCMs, and the model MJOs are often too weak and propagate too fast [e.g., Hayashi and Sumi, 1986; Hayashi and Golder, 1986, 1988; Lau et al., 1988; Slingo et al., 1996; Waliser et al., 2003; Lin et al., 2006]. The Atmospheric Model Intercomparison Project (AMIP) study by Slingo et al. [1996] found that no model has captured the dominance of the MJO in space-time spectral analysis found in observations, and nearly all have relatively more power at higher frequencies (<30 d) than in observations. Recently, Lin et al. [2006] evaluate the tropical intraseasonal variability in 14 coupled GCMs participating in the Intergovernmental Panel on Climate Change (IPCC) Fourth Assessment Report (AR4). The results show that current state-of-the-art GCMs still have significant problems and display a wide range of skill in simulating the tropical intraseasonal vari-

¹NOAA ESRL/CIRES Climate Diagnostics Center, Boulder, Colorado, USA.

²Now at Department of Geography, Ohio State University, Columbus, Ohio, USA.

³Department of Atmospheric Sciences, Seoul National University, Seoul, Korea.

⁴NASA GSFC Global Modeling and Assimilation Office, Greenbelt, Maryland, USA.

Table 1. Description of Sensitivity Experiments

Experiment	Autoconversion Timescale, s
EXP8	19,200
EXP7 (CNTL)	9600
EXP6	6400
EXP5	3200
EXP4	1600
EXP3	800
EXP2	400
EXP1	200
EXP0 (NO CLOUD)	0

ability. Most of the models produce overly weak MJO variance and poor MJO propagation. Moreover, the MJO variance in 13 of the 14 models does not come from a pronounced spectral peak, but usually comes from part of an overreddened spectrum, which in turn is associated with too strong persistence of equatorial precipitation.

[4] *Lin et al.* [2006] also evaluated, for the first time in literature, other convectively coupled equatorial waves

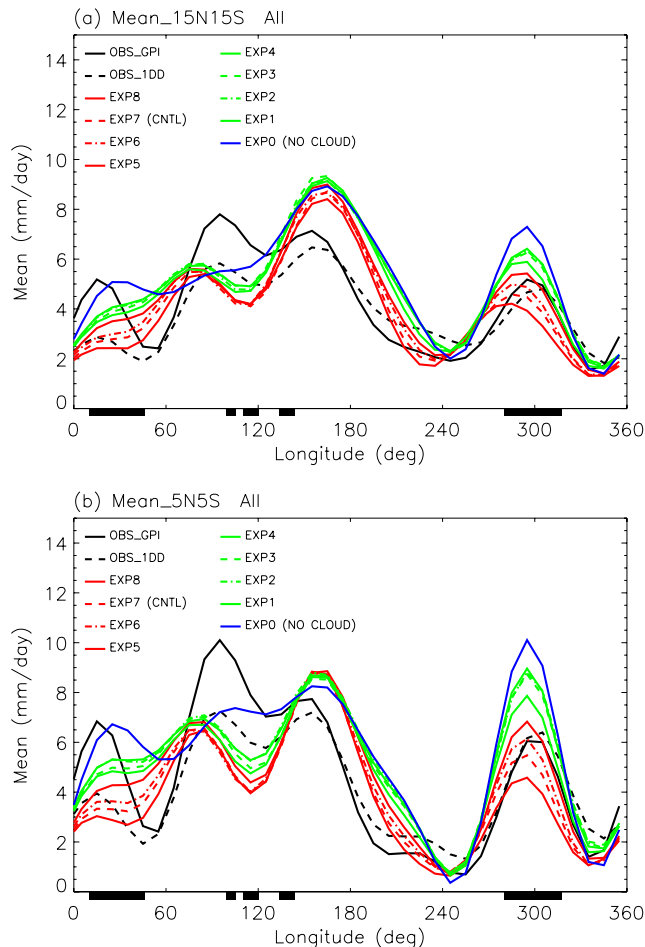


Figure 1. Annual mean precipitation along the equatorial belt averaged between (a) 15°N and 15°S and (b) 5°N and 5°S for two observational data sets and each model experiment. Data are smoothed zonally to keep only wave numbers 0–6. Locations of continents within the equatorial belt are indicated by black bars under the abscissa.

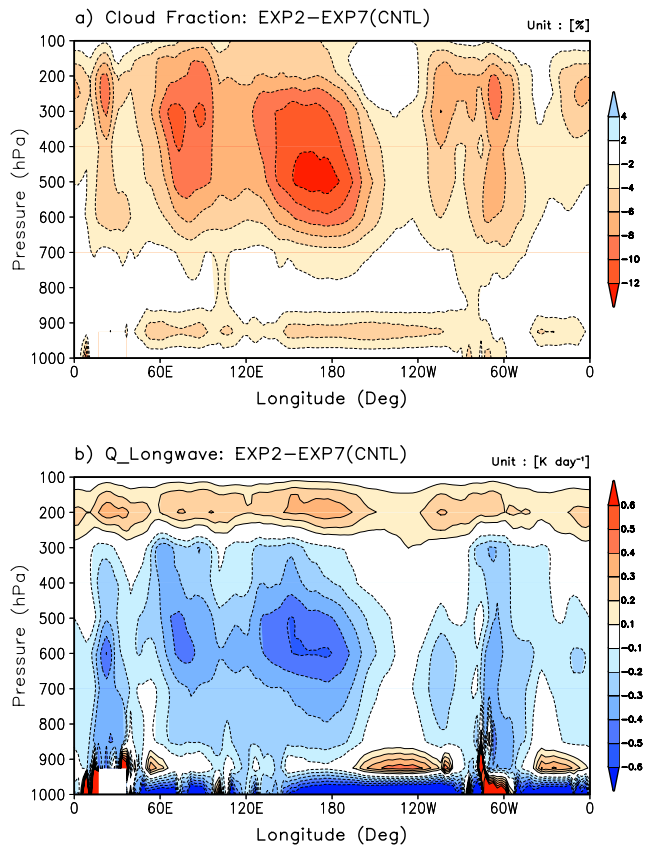


Figure 2. Height-longitude cross section of EXP2-EXP7 difference in annual mean (a) cloud fraction, (b) longwave heating, (c) shortwave heating, and (d) total radiative heating averaged between 20°N–20°S.

simulated by the GCMs. About half of the models have signals of convectively coupled equatorial waves, with Kelvin and MRG-EIG waves especially prominent. However, the variances are generally too weak for all wave modes except the $n = 0$ EIG wave, and the phase speeds are generally too fast, suggesting that these models may not have a large enough reduction in their “effective static stability” by diabatic heating.

[5] It is widely accepted that wave-heating feedback is central for the amplification and maintenance of the convectively coupled equatorial waves. The total diabatic heating has two main components: convective heating (release of latent heat, along with eddy flux divergences that shape the profile) and radiative heating. Most theoretical studies have focused only on the role of convective heating in wave-heating feedback. The mechanisms studied include the wave–conditional instability of the second kind (wave-CISK) mechanism [e.g., *Lau and Peng*, 1987], the frictional wave-CISK mechanism [e.g., *Wang and Rui*, 1990], the wind-induced surface heat exchange (WISHE) mechanism [e.g., *Emanuel*, 1987; *Neelin et al.*, 1987], and the charge-discharge mechanism [e.g., *Bladé and Hartmann*, 1993; *Hayashi and Golder*, 1997].

[6] The radiative heating, on the other hand, also contributes significantly to the total diabatic heating and thus may affect the convectively coupled equatorial waves. The radiative heating may be conveniently separated into two

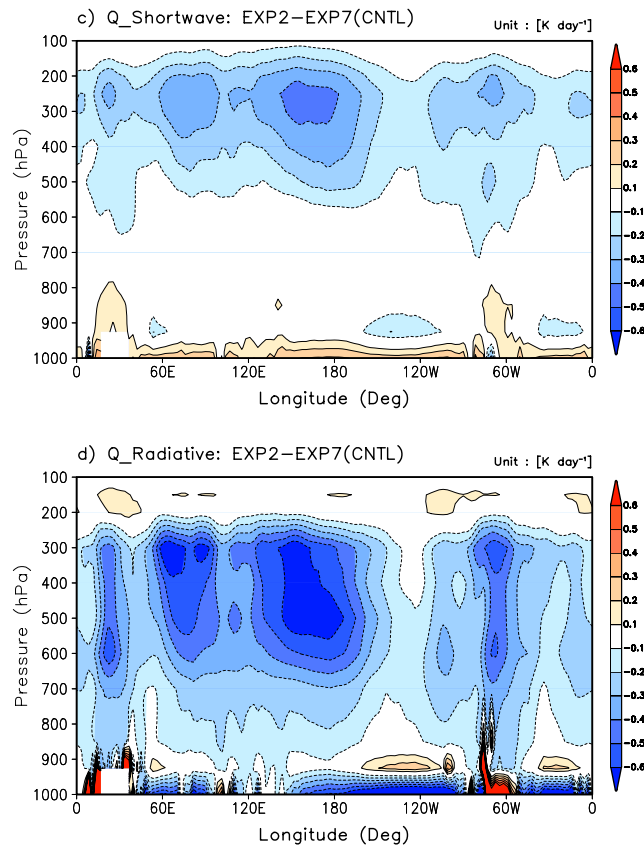


Figure 2. (continued)

components, column-integrated heating and vertical-heating profile, which have different effects on deep convection. The column-integrated heating tends to enhance the convective heating because in the convectively active phase of a convectively coupled equatorial wave, clouds and water vapor associated with deep convection reduce outgoing longwave radiation (OLR) to space and therefore increase radiative heating in the atmosphere. As a quantitative measure, an enhancement factor of radiative heating can be defined as the ratio between the column-integrated radiative heating and the column-integrated convective heating. Using collocated top-of-atmosphere (TOA) and surface-radiative flux measurements from special field program data and long-term TOA flux data, *Lin and Mapes [2004]* examined the column-integrated radiation budget of the MJO and found that the column-integrated radiative heating is nearly in phase with the precipitation and enhances the net condensation heating by about 10–15%, with the dominant contribution from the reduction of OLR during wet periods. Recently, several modeling studies found that radiative heating can also significantly affect the amplitude and/or phase speed of the simulated intraseasonal oscillations [e.g., *Raymond, 2001; Sobel and Gildor, 2003; Bony and Emanuel, 2005*]. In an idealized model of thermodynamic atmosphere-ocean interaction on the intraseasonal timescale, *Sobel and Gildor [2003]* found that the enhancement factor of radiative heating is the most sensitive parameter, and both the growth rate and the period of simulated intraseasonal oscillations increase with the enhancement factor. In a theoretical model, *Raymond [2001]*

demonstrated that when the enhancement factor is very large, the radiative heating can reduce the effective static stability to a negative value, that is, to an effective static instability. He termed this instability the radiative-convective instability. An MJO-like slow eastward propagating mode appears to develop in his model from this radiative-convective instability.

[7] The second aspect of radiative heating is its vertical-heating profile. Using the TOGA COARE radiative heating profiles calculated by *Qian [2003]*, *Lin et al. [2004]* analyzed the vertical structure of radiative heating in the MJO. They found that during the convectively active phase, radiative heating is characterized by warming in the lower and middle troposphere but cooling in the upper troposphere. Such a heating profile tends to suppress deep convection, in contrast to the enhancing effect of column-integrated heating. Several previous GCM studies found that cloud-radiative heating tends to suppress the simulated MJO-like mode [e.g., *Slingo and Madden, 1991; Lee et al., 2001; Lau et al., 2005*]. *Lee et al. [2001]* conducted two types of simulation: one with prescribed zonal mean radiation and the other with fully interactive clouds and radiation. In contrast to the fixed radiation case, where the MJO is simulated reasonably well, the cloud radiation interaction significantly contaminates the eastward propagation of the MJO by producing small-scale disturbances moving westward with the easterly basic winds. The small-scale dis-

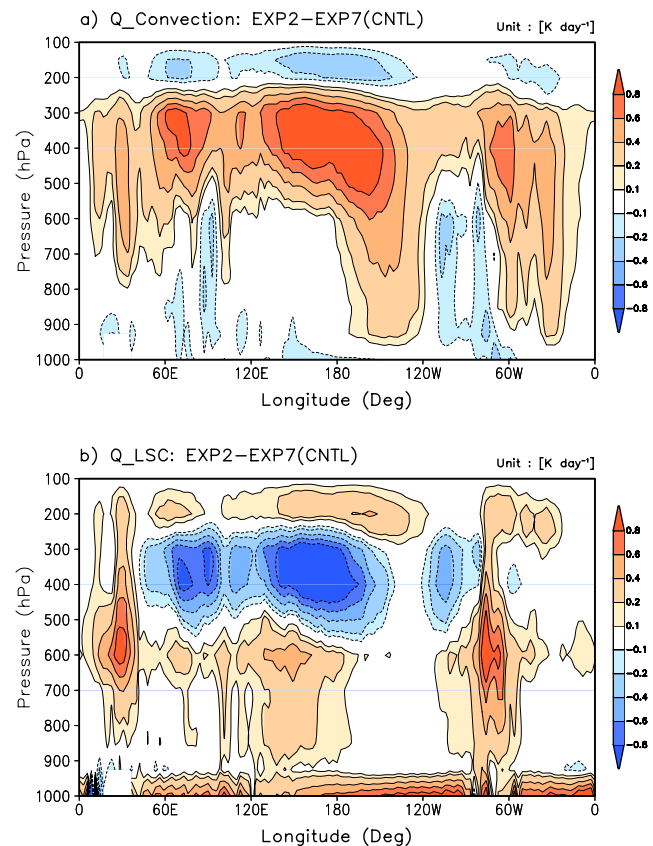


Figure 3. Same as Figure 2 but for (a) convective heating, (b) large-scale condensational heating, (c) total heating due to moist processes, and (d) total diabatic heating.

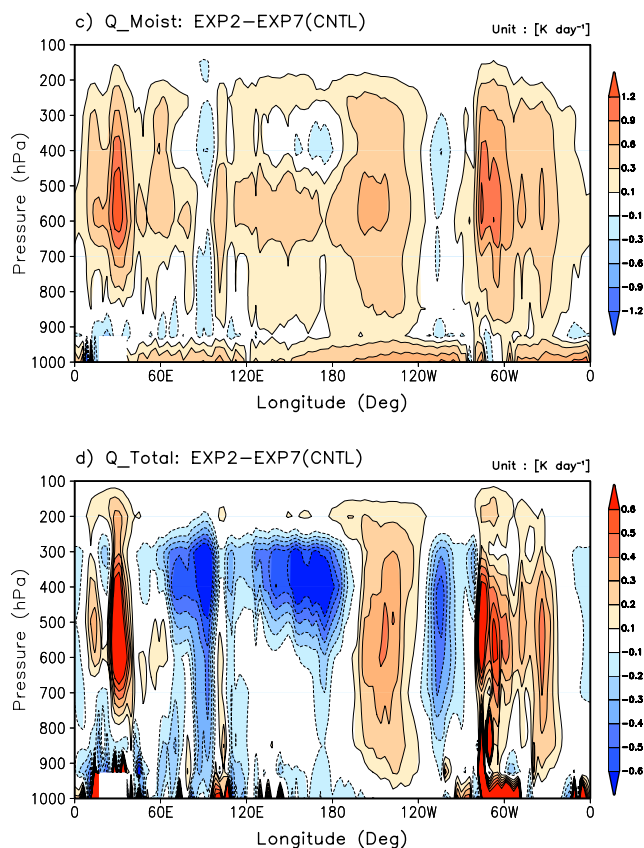


Figure 3. (continued)

turbances are persistently excited by a strong positive feedback through interaction between cumulus-anvil clouds and radiation. The longwave interaction is shown to play a bigger role in contaminating the MJO than the shortwave interaction does. The anvil clouds reduce the longwave cooling significantly in the lower troposphere while releasing latent heating in the upper troposphere. To moderate the strong cloud radiation feedback, the large-scale condensation scheme in the GCM is modified by reducing the autoconversion timescale, needed for cloud condensates to grow up to raindrops. In addition, upper air ice cloud contents are reduced to change the cloud albedo. These modifications make a more realistic simulation of the MJO similar to the observed. However, the effects of cloud-radiative heating on atmospheric general circulation model (AGCM)-simulated other convectively coupled equatorial waves (e.g., Kelvin, $n = 1$ ER, and MRG waves) have not been studied.

[8] The purpose of this study is to extend the *Lee et al.* [2001] study to examine the effects of cloud-radiative heating on AGCM-simulated convectively coupled equatorial waves. Following *Lee et al.* [2001], the strength of cloud-radiative heating is adjusted by modifying the autoconversion timescale, needed for cloud condensates to grow up to raindrops. The questions we address are as follows: Are the AGCM-simulated convectively coupled equatorial waves sensitive to the strength of cloud-radiative heating? Does cloud-radiative heating enhance or suppress the waves?

[9] The models and validation data sets used in this study are described in section 2. The diagnostic methods are described in section 3. Results are presented in section 4. A summary and discussion are given in section 5.

2. Models and Validation Data Sets

[10] The model used in this study is the Seoul National University atmospheric general circulation model (SNUGCM). The model is a global spectral model, with 20 vertical levels in a sigma coordinate. In this study, T42 ($\sim 2.8^\circ \times 2.8^\circ$) truncation is used for the model horizontal resolution. Moist convection is represented by the simplified version of the Relaxed Arakawa-Schubert (RAS) formulation [*Numaguti et al.*, 1995]. The large-scale condensation scheme consists of a prognostic microphysics parameterization for total cloud liquid water [*Le Treut and Li*, 1991] with a diagnostic cloud fraction parameterization. Nonprecipitating shallow convection scheme [*Tiedtke*, 1983] is also implemented in the model for the midtropospheric moist convection. The boundary layer scheme is a nonlocal diffusion scheme based on the work of *Holtstlag and Boville* [1993], while the land surface model is from *Bonan* [1998]. The radiation process is parameterized by the two-stream k distribution scheme implemented by *Nakajima et al.* [1995]. Other details of the model physics are described by *Lee et al.* [2001, 2003].

[11] To examine the effects of cloud-radiative heating on the simulated convectively coupled equatorial waves, we

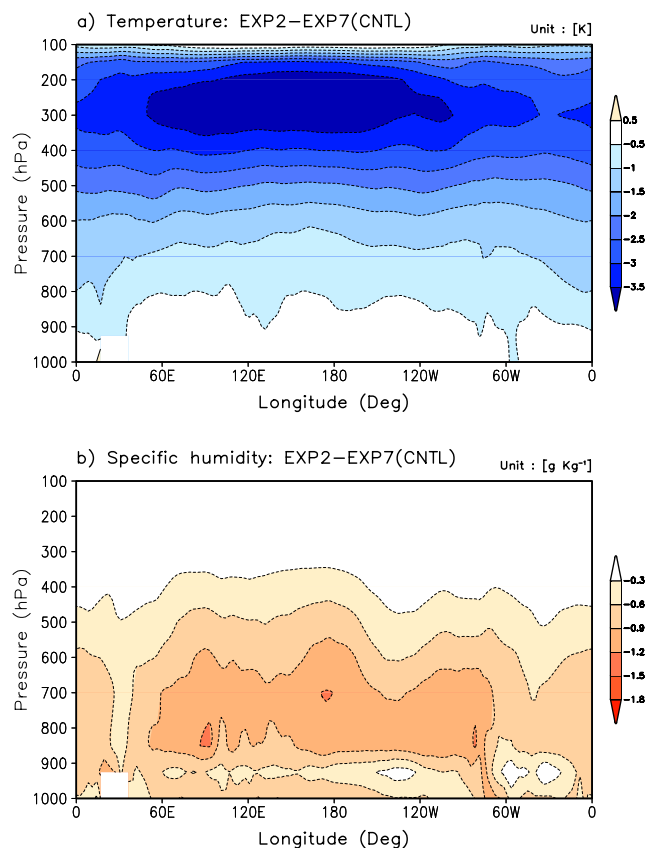


Figure 4. Same as Figure 2 but for (a) temperature and (b) specific humidity.

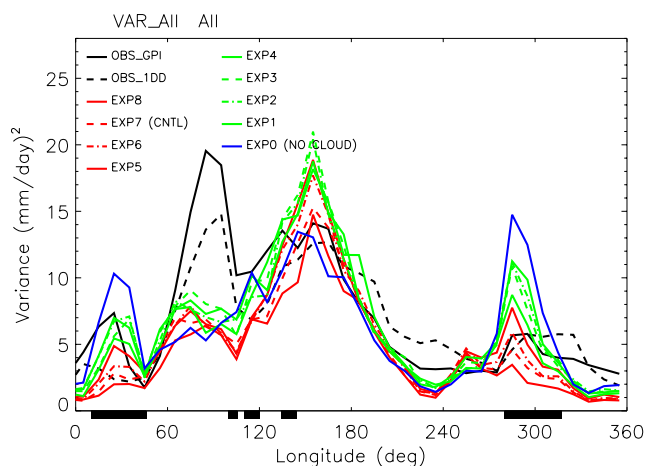


Figure 5. Variance of the 2–128 d precipitation anomaly along the equator averaged between 15°N–15°S.

tested the parameter sensitivity to the autoconversion timescale in the large-scale condensation scheme. As discussed by *Lee et al.* [2001], this parameter gives a characteristic time for autoconversion of cloud droplets into precipitating raindrops. As it becomes smaller, the precipitating process is faster with shorter cloud lifetime, which can effectively reduce the magnitude of the cloud-radiative heating [*Lee et al.*, 2001]. In this study a wide range of autoconversion timescales were tested for the timescale originally set to 9600 s, which are listed in Table 1. In particular, we conducted a “no cloud” experiment (EXP0) in which all the condensates by cumulus convection and large-scale condensation precipitate out instantaneously. In each experiment the minimum entrainment constraint in the RAS convection scheme was commonly applied with a positive constant $\alpha = 0.1$, which is the same as by *Lee et al.* [2001]. Each run consists of 8-year (a) AMIP-style simulations (1997–2004) driven by the same observed sea surface temperatures and sea ice distributions.

[12] The model simulations are validated using multiple observational data sets. To bracket the uncertainties associated with precipitation measurements/retrievals, especially the well-known difference between infrared (IR) based retrievals and microwave-based retrievals [e.g., *Yuter and Houze*, 2000], we use two different precipitation data sets: (1) 8 a (1997–2004) of daily GOES Precipitation Index (GPI) [*Janowiak and Arkin*, 1991] precipitation with a horizontal resolution of 2.5 degree longitude by 2.5 latitude, which is retrieved on the basis of IR measurements from multiple geostationary satellites; and (2) 8 a (1997–2004) of daily Global Precipitation Climatology Project (GPCP) One-Degree-Daily (1DD) Precipitation [*Huffman et al.*, 2001] with a horizontal resolution of 1 degree longitude by 1 degree latitude. These are IR-based GPI retrievals scaled by the monthly means of microwave-based SSM/I retrievals.

3. Method

[13] Through the space-time spectral analysis of outgoing longwave radiation (OLR), *Takayabu* [1994] and WK demonstrated that a significant portion of tropical cloudiness is organized in corresponding to the normal

modes of the linear shallow water system isolated by *Matsuno* [1966]. In WK, these spectra represent the power remaining in the symmetric and antisymmetric components of OLR about the equator after dividing raw wave number–frequency power spectra by an estimate of the background power spectrum. Peaks standing above the background correspond to the Kelvin, $n = 1$ ER, MRG, $n = 0$ EIG, $n = 1$ WIG, and $n = 2$ WIG waves. It was found that the dispersion curves that best match the wave number–frequency characteristics of these waves have surprisingly shallow equivalent depths in the range of around 25 m, which is about an order of magnitude smaller than that expected for a free wave with a similar vertical wavelength twice the depth of the troposphere [e.g., *Salby and Garcia*, 1987; *Wheeler et al.*, 2000].

[14] Using the methodology of WK, space-time spectra of daily tropical precipitation were obtained for the 8 a of model data used in this study and compared with those of 8 a of observed precipitation estimates from the GPI and 1DD data sets. We will briefly outline this procedure here, and refer the reader to WK and *Lin et al.* [2006] for further details.

[15] The model and validation precipitation data were first interpolated to a zonal resolution of 5 degrees longitude with the latitudinal resolution. We first decomposed the precipitation into its antisymmetric and symmetric components, averaged these from 15°N to 15°S, and computed spectra of the averaged values. To reduce noise, the space-time spectra were calculated as in WK for successive overlapping segments of data and then averaged, here 128 d long with 78 d of overlap between each segment. Complex Fourier coefficients are first obtained in zonal planetary wave number space, which are then subjected to a further complex FFT to obtain the wave number–frequency spectrum for the symmetric and antisymmetric components of precipitation about the equator.

[16] An estimate of the “background” space-time spectrum is obtained for each data set by averaging the power of the symmetric and antisymmetric spectra and smoothing this by successive passes of a 1-2-1 filter in frequency and wave number (see WK). The raw spectra are then divided by this background to obtain an estimate of the signal standing above the background noise. Here we assume the signal is significant if it stands at 1.2 times (or 20% above) the background. It should be emphasized that, while this is only a rough estimate of the true “significance” of the signals, the intent is to simply identify those modes which might represent signals in rainfall standing above a simple red noise continuum that would presumably prevail if rainfall were not organized by disturbances on the large scale.

[17] The definitions of Kelvin, $n = 1$ ER, MRG, $n = 0$ EIG, and $n = 1$ WIG modes are as by WK and *Lin et al.* [2006]. Each mode was isolated by filtering in the wave number–frequency domain (see WK, Figure 6, for the defined regions of filtering for each wave), and the corresponding time series were obtained by an inverse space-time Fourier transform.

[18] As by *Lin et al.* [2006], the MJO is defined as significant rainfall variability in eastward wave numbers 1–6 and in the period range of 30–70 d. The variance of the MJO anomaly was also compared with the variance of its

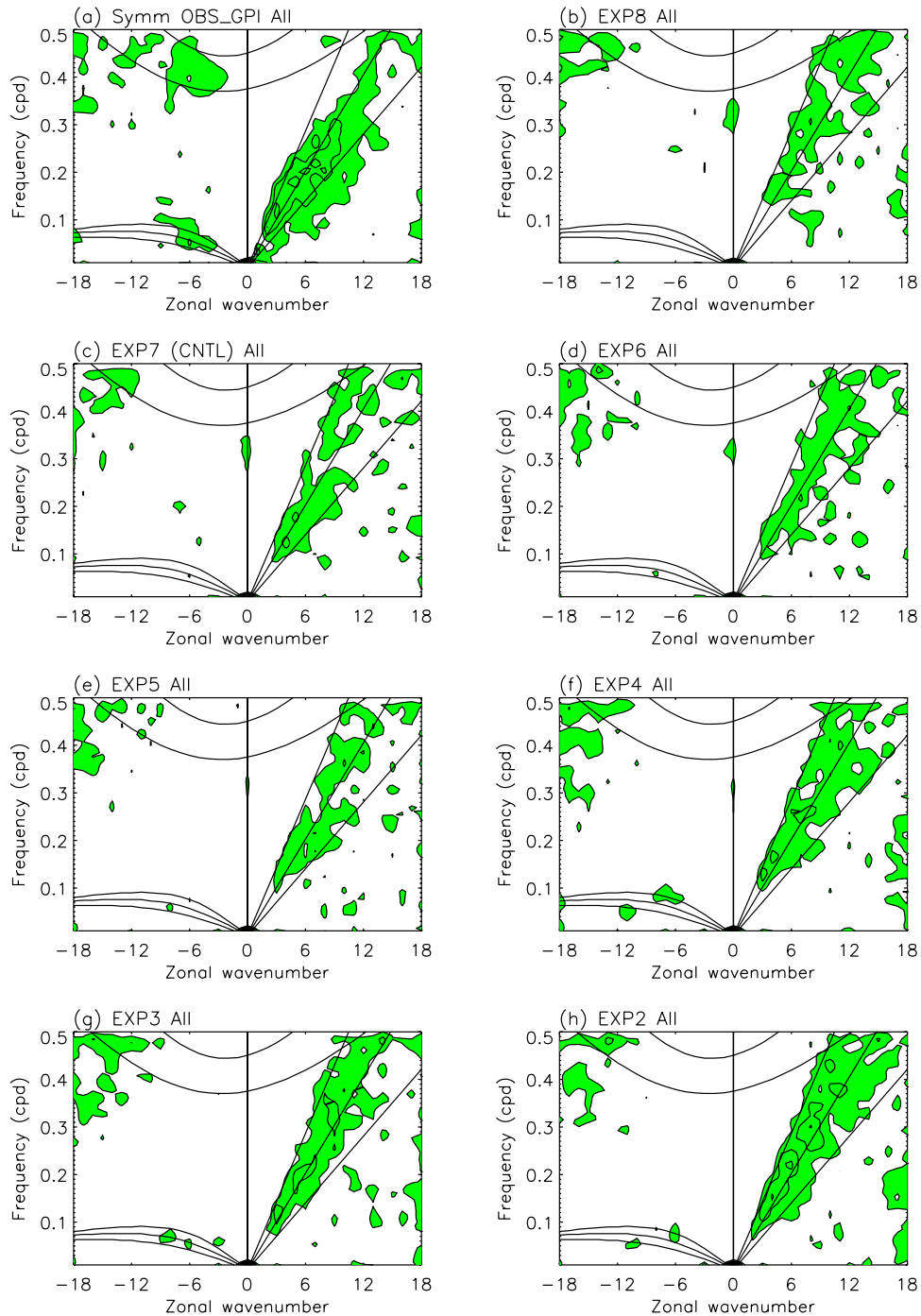


Figure 6. Space-time spectrum of 15°N – 15°S symmetric component of precipitation divided by the background spectrum. Superimposed are the dispersion curves of the odd meridional mode-numbered equatorial waves for the five equivalent depths of 12, 25, and 50 m. Frequency spectral width is $1/128$ cpd.

westward counterpart, i.e., the westward wave numbers 1–6, 30–70 d anomaly, which was isolated using the same method as above.

[19] It is important to note that the diabatic heating processes are generally nonlinear, and the equatorial wave mode decomposition approach is an approximation of the convectively coupled modes based on the concept of the free modes with proper adjustment of the equivalent depth. Nonlinear dynamical processes also play a significant role in the organization, so the heating associated with one

particular mode (as isolated by the above linear decomposition method) is determined not only by the mode itself, but also by the time-mean field and the rectification effects of subscale modes.

4. Results

4.1. Climatological Precipitation in the Equatorial Belt

[20] Previous observational studies indicate that the intra-seasonal variance of convection is highly correlated with

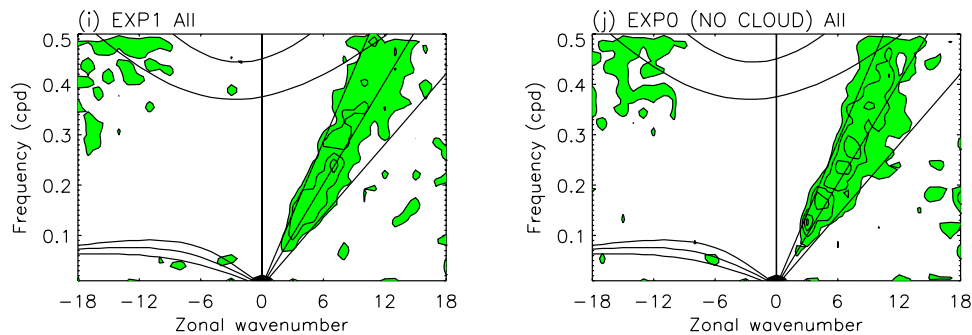


Figure 6. (continued)

time-mean convective intensity [e.g., Hendon *et al.*, 1999; WK]. Therefore we first look at the 8 a time-mean precipitation along the equatorial belt, especially over the Indo-Pacific warm pool region, where most of the convectively coupled equatorial waves have the largest variance (WK). Figure 1 shows the annual mean precipitation versus longitude averaged between 15°N and 15°S (Figure 1a) and 5°N and 5°S (Figure 1b). To focus on the large-scale features, we smoothed the data zonally to retain only zonal wave numbers 0–6. Figure 1 demonstrates two points. First, all experiments simulate reasonably the basic feature of observed precipitation, with the primary maximum over the Indo-Pacific warm pool region and a secondary local maximum over Central/South America. Within the warm pool region all experiments also reproduce the local minimum of precipitation over the maritime continent, but there is a positive bias over the western Pacific and a negative bias over the eastern Indian Ocean. Outside the warm pool region all experiments produce quite realistic magnitude of precipitation over Central/South America. Comparing with the 15°N – 15°S average (Figure 1a), the biases in 5°N – 5°S average (Figure 1b) are smaller over western Pacific, but larger over eastern Indian Ocean. Second, changing the autoconversion rate does not change much the mean precipitation over the Indo-Pacific warm pool region, and thus any difference in the intraseasonal variability in this region is likely due to change in cloud radiation feedback instead of change in mean precipitation. Outside the warm pool region, increasing the autoconversion rate significantly increases mean precipitation over the continents of Africa and South America.

[21] Although changing the autoconversion rate does not change much the time-mean precipitation over the Indo-Pacific warm pool region, it significantly changes the time-mean clouds, radiative heating, and vertical structure of the tropical atmosphere. As an example, Figure 2 shows the longitude-height cross section of EXP2–EXP7 difference in annual mean cloud amount (Figure 2a), longwave heating rate (Figure 2b), shortwave heating rate (Figure 2c), and total radiative heating rate (Figure 2d) averaged between 20°N – 20°S . Increasing autoconversion rate substantially reduces the annual mean cloud amount in the upper troposphere and to a lesser extent in the lower troposphere near the surface (Figure 2a). The decrease in cloud amount leads to reduction in longwave heating rate near the cloud base, but increase in longwave heating rate at the cloud top (Figure 2b). It also leads to increase of shortwave heating

rate in the upper part of the clouds (Figure 2c), which largely cancels the increase of longwave heating there. Therefore the total radiative heating decreases both in the upper troposphere and near the surface (Figure 2d).

[22] The changes in autoconversion rate and radiative heating also lead to changes in moist processes and associated heating (Figure 3). The heating due to convection (Figure 3a) increases in the upper troposphere between 300–600 mb, but decreases near the tropopause. On the other hand, the heating due to large-scale condensation (Figure 3b) often shows sign opposite to that due to deep convection, with decrease in the upper troposphere between 250–500 mb but increase both near the tropopause and in the lower troposphere. When they are added together, the total heating due to moist processes slightly increases throughout the troposphere in many regions (Figure 3c), which is not large enough to compensate the decrease of radiative heating in the warm pool region (Figure 2d). Therefore the total diabatic heating decreases in the upper troposphere in the warm pool region (Figure 3d).

[23] The change in diabatic heating leads to change in temperature (Figure 4a), which is characterized by a significant cooling in the upper troposphere. The temperature change is more spatially homogeneous than other fields, which may be caused by the very weak Coriolis force near the equator, leading to very weak pressure gradient and temperature gradient. This is often referred to as the “weak temperature gradient” hypothesis in theoretical models [e.g., Sobel and Bretherton, 2000; Bretherton and Sobel, 2002; Majda and Klein, 2003]. Consistent with enhancement of convection (Figure 3a) and large-scale condensation (Figure 3b), the humidity change (Figure 4b) is characterized by significant drying in the lower troposphere.

[24] The above results shown in Figures 2–4 are for the differences between EXP2 and EXP7 (control run). Other experiments with autoconversion rate higher than EXP7 generally show pattern of differences similar to EXP7, while the EXP8 experiment, which has an autoconversion rate lower than EXP7, shows the opposite sign of differences (not shown). The whole picture is quite consistent with the results of Lau *et al.* [2005], with our EXP2 similar to their E1 experiment and our EXP7 similar to their E2 experiment. Lau *et al.* [2005] did a detailed analysis of the microphysical mechanism for the changes in mean state, and found that a faster autoconversion rate leads to more warm rain, which produces more condensational heating in the lower troposphere. The vertical differential heating

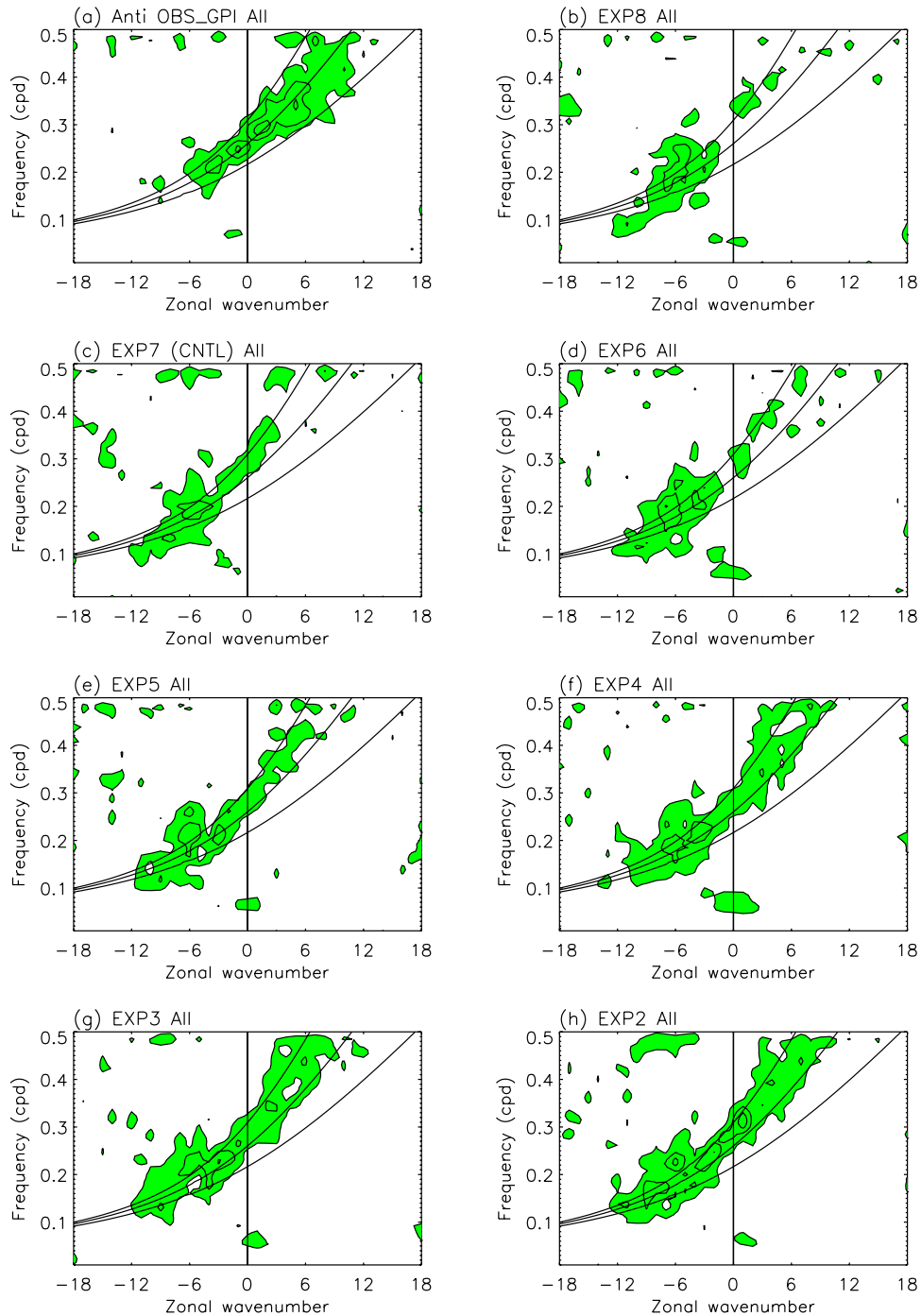


Figure 7. As in Figure 6 except for 15°N – 15°S antisymmetric component of precipitation.

between condensational heating in the lower troposphere and radiative cooling in the upper troposphere destabilizes the tropical atmosphere, producing a positive feedback via secondary circulation between convective tower and anvil regions (cold rain), and adjacent middle-to-low-cloud (warm rain) regions. Because the focus of the present study is on tropical intraseasonal variability rather than the mean state, we will not repeat the analysis of *Lau et al.* [2005] but refer the interested reader to their paper for more detailed analysis of the underlying microphysical mechanism.

[25] To summarize, the climatological precipitation over the Indo-Pacific warm pool is reasonably simulated by all experiments. Changing the autoconversion rate has little effect on the climatological mean precipitation, suggesting that any related change in intraseasonal variability is likely due to change in cloud radiation feedback instead of change in mean precipitation. Nevertheless, increasing autoconversion rate significantly reduces the time-mean clouds and radiative heating both in the upper troposphere and near the surface and enhances heating due to moist processes in the middle troposphere. These lead to cooling of time-mean

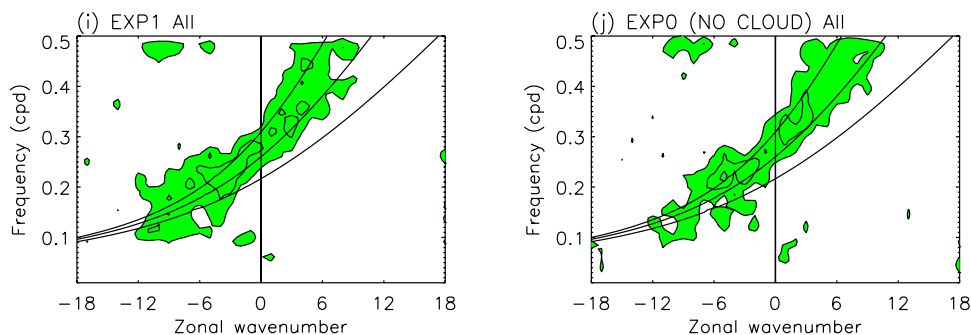


Figure 7. (continued)

upper troposphere temperature and drying of lower-troposphere moisture. As will be shown in section 4.4, the changes in time-mean thermodynamical structure affect the wave-heating feedback in the convectively coupled equatorial waves.

4.2. Total Intraseasonal (2–128 d) Variance

[26] Figure 5 shows the total variance of the 2–128 d filtered precipitation anomaly along the equator averaged between 15°N–15°S. There are two important things to note concerning Figure 5. First, the total intraseasonal variance in most experiments is overly large over western Pacific, although it is overly small over Indian Ocean. This is very encouraging because 13 of the 14 IPCC AR4 GCMs analyzed by *Lin et al.* [2006] produce overly small variance over both western Pacific and Indian Ocean, although their annual mean precipitation is often as large as in the SNU model studied here. Second, increasing the autoconversion rate (i.e., reducing cloud-radiative heating) tends to enhance the total intraseasonal variance over western Pacific, Indian Ocean, South America, and Africa. The enhancement is not always monotonic. For example, EXP0 (the “no cloud” experiment) produces less variance than most of the other experiments over western Pacific.

4.3. Dominant Intraseasonal Modes

[27] Figures 6 and 7 show the results of dividing the symmetric and antisymmetric raw spectra by the estimates of their background spectra. This normalization procedure removes a large portion of the systematic biases within the various models and observed data sets, more clearly displaying the model disturbances with respect to their own climatological variance at each scale. Signals of the Kelvin, $n = 1$ ER, and $n = 1$ WIG waves are readily identified in the observational symmetric spectra (Figure 6a), along with the MRG and $n = 0$ EIG waves in the antisymmetric spectra (Figure 7a). Dispersion curves of the shallow water modes are also shown on all spectra, corresponding to equivalent depths of 12, 25, and 50 m. As in the OLR spectra of WK, all of the observed spectral peaks corresponding to shallow water modes best match an equivalent depth of around 25 m in the observational rainfall data.

[28] The model spectra in Figures 6 and 7 demonstrate three points. First, many experiments produce pronounced signals of convectively coupled equatorial waves, with Kelvin and MRG-EIG waves especially prominent. The phase speed is quite realistic for all the wave modes except

the $n = 0$ EIG wave which displays a too fast phase speed. These support our use of the SNUGCM to examine the effect of cloud radiation feedback on the waves. Second, increasing the autoconversion rate significantly enhances the prominence of the Kelvin and $n = 0$ EIG waves. Third, changing the autoconversion rate has little effect on the phase speed of the waves.

[29] When a model displays signals of a certain wave mode in Figures 6 and 7, it means that the variance of that wave mode stands out above the background spectra (i.e., a high signal-to-noise ratio), but the absolute value of the variance of that wave mode may not be large. Therefore it is of interest to look further at the absolute values of the variance of each wave mode. Figure 8 shows the variances of the MJO (Figure 8a), Kelvin (Figure 8b), $n = 1$ ER (Figure 8c), MRG (Figure 8d), $n = 0$ EIG (Figure 8e), and $n = 1$ WIG modes (Figure 8f) along the equator averaged between 15°N and 15°S. Figure 8 demonstrates four points. First, increasing the autoconversion rate tends to enhance significantly the variance of the Kelvin wave (Figure 8b), ER wave (Figure 8c), MRG wave (Figure 8d), and $n = 1$ WIG wave (Figure 8f), and the model variance for very fast autoconversion rate sometimes approaches the observed variance. This is encouraging because among the 14 IPCC AR4 GCMs analyzed by *Lin et al.* [2006], only a couple of models produce wave variances approaching the observed values. Second, the increase of variance for the above waves is not always monotonic with increasing autoconversion rate. In particular, EXP0 (the “no cloud” experiment) often produces weaker variance than EXP1 and EXP2. This is probably due to some nonlinear processes associated with cloud microphysics, radiation, or convection. Third, changing autoconversion rate does not change much the variance of the MJO (Figure 8a), which is always much smaller than the observed value. This further illustrates that MJO, as a combined Kelvin-Rossby mode [e.g., *Salby and Hendon, 1994*], has quite different dynamics from the Kelvin mode. Fourth, changing autoconversion rate does not affect systematically the variance of $n = 0$ EIG wave (Figure 8e), which is larger than the observed value in most of the experiments. This is consistent with the finding of *Lin et al.* [2006] that most of the IPCC AR4 models can produce large variance for $n = 0$ EIG wave although they produce very weak variance for other waves. In other words, the variance of $n = 0$ EIG wave seems to be independent of model physics, which is very interesting and needs further studies in the future.

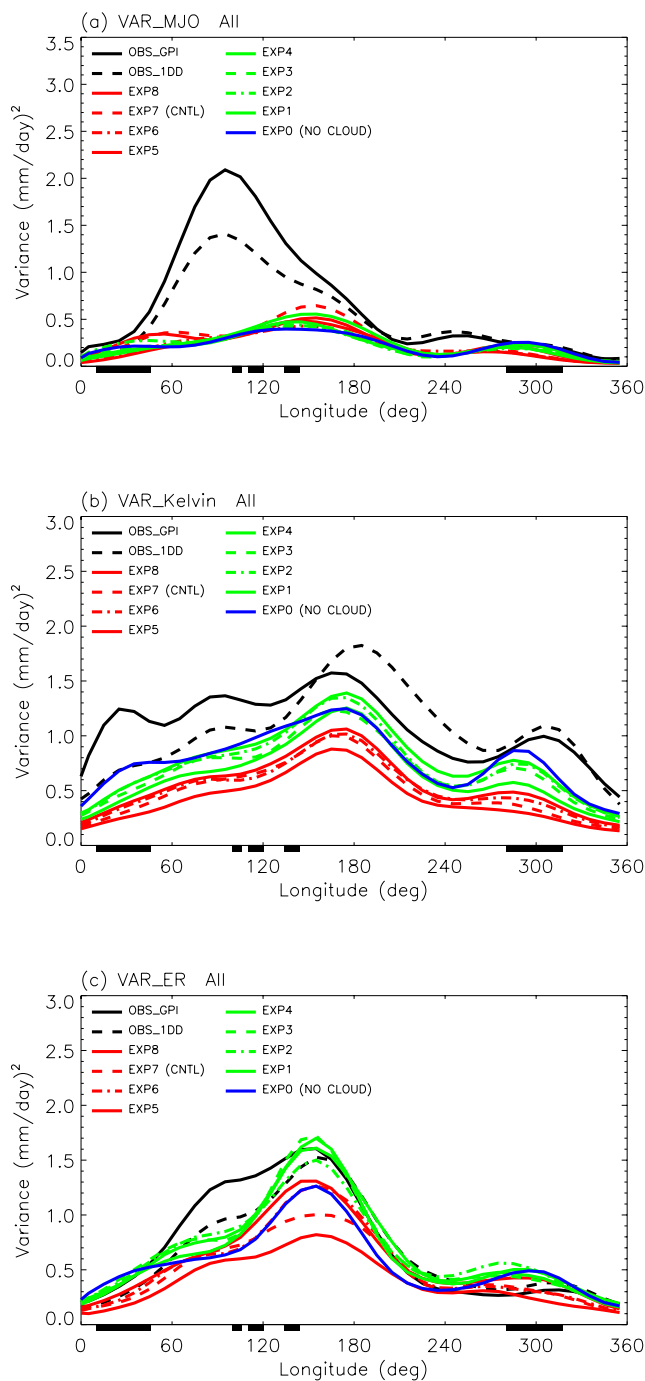


Figure 8. Variances of (a) Madden-Julian Oscillation (MJO), (b) Kelvin, (c) $n = 1$ equatorial Rossby (ER), (d) mixed Rossby-gravity (MRG), (e) $n = 0$ eastward inertial gravity (EIG), and (f) $n = 1$ westward inertial gravity (WIG) modes along the equator averaged between 15°N and 15°S .

[30] In summary, all experiments produce prominent signals of convectively coupled equatorial waves, with Kelvin and MRG-EIG waves especially prominent and the phase speeds generally quite realistic. These support our use of the SNUGCM to examine the effect of cloud radiation feedback on the convectively coupled equatorial waves. Increasing autoconversion rate enhances the prominence

of Kelvin and $n = 0$ EIG waves. It also tend to enhance significantly the variance of the Kelvin, ER, MRG, and $n = 1$ WIG waves, but not the MJO or $n = 0$ EIG wave. Changing autoconversion rate has little effect on the phase speed of the waves.

4.4. Vertical Structure of Diabatic Heating and Wave-Heating Feedback

[31] To further understand the effects of changing autoconversion rate on simulations of convectively coupled equatorial waves, we first analyze in this subsection the vertical structure of diabatic heating at the intraseasonal

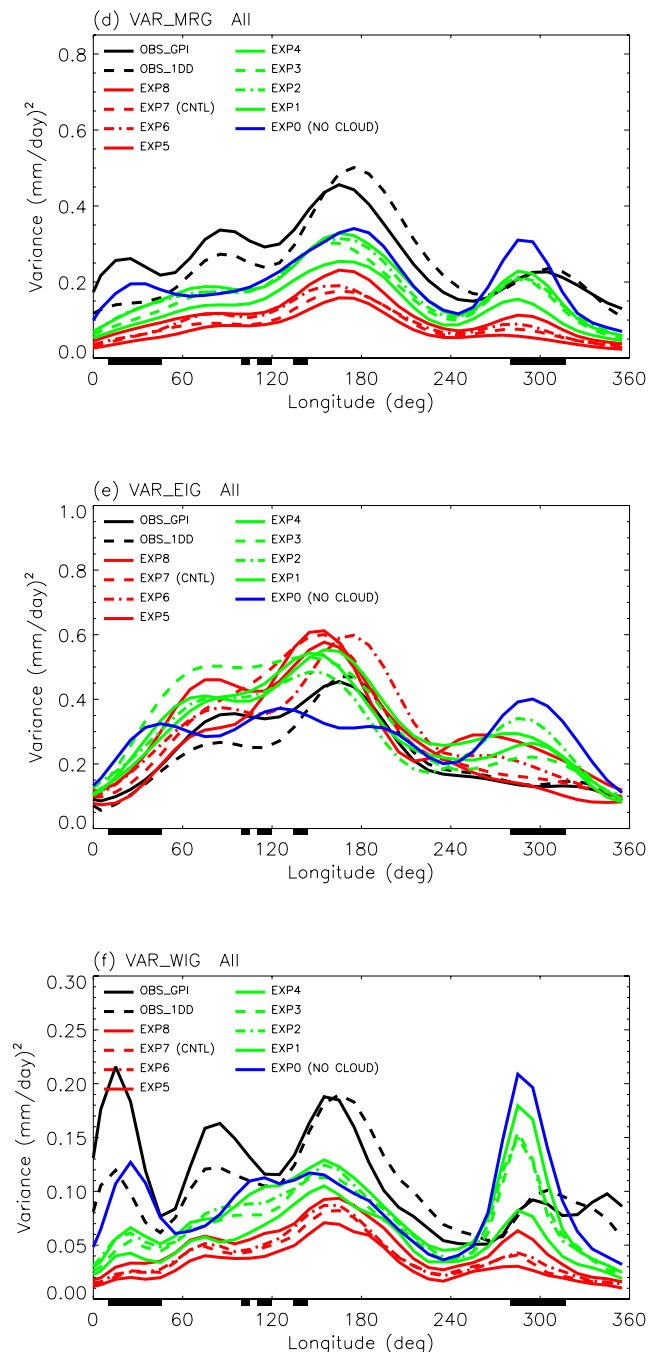


Figure 8. (continued)

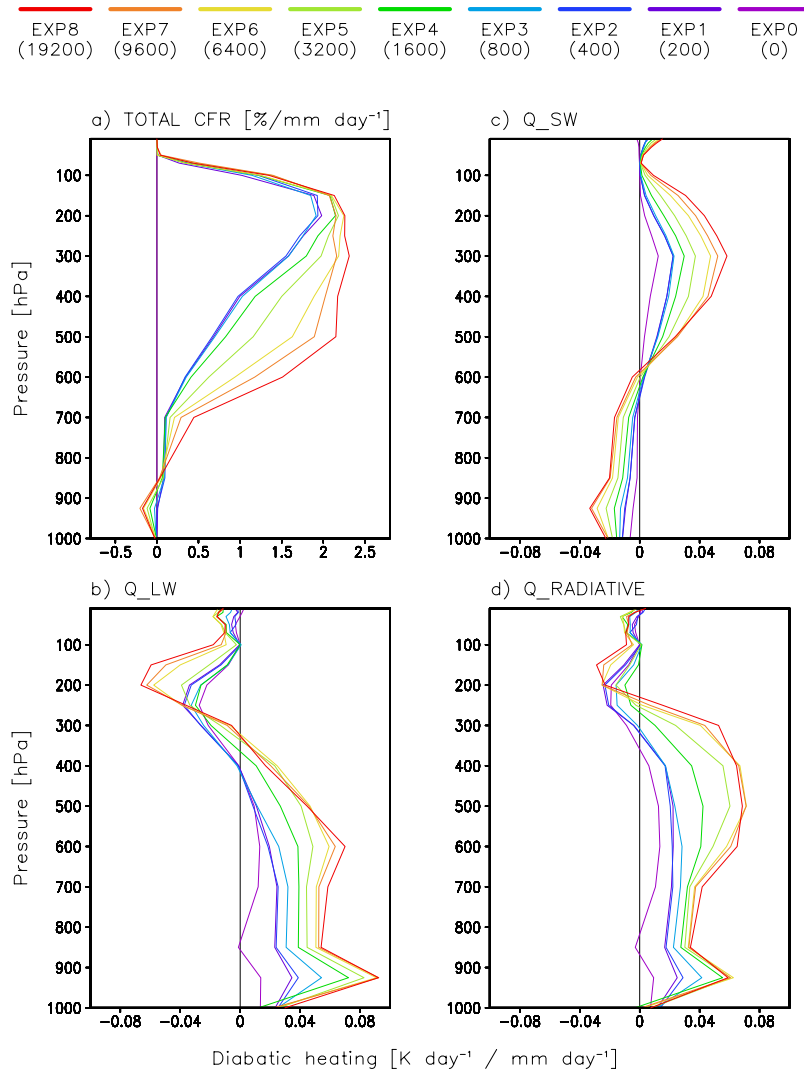


Figure 9. Linear regression against surface total precipitation for (a) cloud fraction, (b) shortwave heating, (c) longwave heating, and (d) total radiative heating.

timescale, including both the radiative heating and heating due to moist processes. Figure 9 shows the linear regression against daily surface precipitation for the vertical profiles of cloud amount (Figure 9a), shortwave heating rate (Figure 9b), longwave heating rate (Figure 9c), and total radiative heating rate (Figure 9d). Increasing autoconversion rate significantly reduces the cloud amount in the upper and middle troposphere, but slightly increases the cloud amount in the lower troposphere (Figure 9a). The reduction of clouds between 200–800 mb leads to weakening of longwave cloud top cooling and cloud base warming (Figure 9b), as well as shortwave in-cloud warming and below-cloud cooling (Figure 9c). Therefore the total radiative heating is significantly reduced between 250 mb and 950 mb, but is slightly increased above 250 mb, and remains almost unchanged near the surface (Figure 9d). The vertically integrated radiative heating per unit precipitation, which is the enhancement factor discussed in the introduction, is thus decreased.

[32] The reduction of radiative heating in most of the free troposphere, together with the almost unchanged radiative

heating near the surface, tends to increase the convective instability. Indeed, the deep convection penetrates to a higher altitude (Figure 10a). However, reduction of upper level clouds leads to significant weakening of the large-scale condensation process and associated upper tropospheric warming/lower-tropospheric cooling (Figure 10b). Therefore the vertical profile of total heating due to moist processes becomes less top-heavy with increasing autoconversion rate (Figure 10c). The total diabatic heating (radiative heating plus heating due to moist processes), usually referred to as Q_1 , just becomes smaller per unit precipitation but with no significant change in its top-heaviness (Figure 10d).

[33] How do the changes in diabatic heating structure affect the convectively coupled equatorial waves? As discussed in the introduction, most of the theories of convectively coupled equatorial waves emphasize the role of wave-heating feedback in determining the phase speed and amplitude of the waves [e.g., Lau and Peng, 1987; Emanuel, 1987; Neelin et al., 1987; Wang and Rui, 1990; Bladé and Hartmann, 1993; Hayashi and Golder, 1997; Raymond,

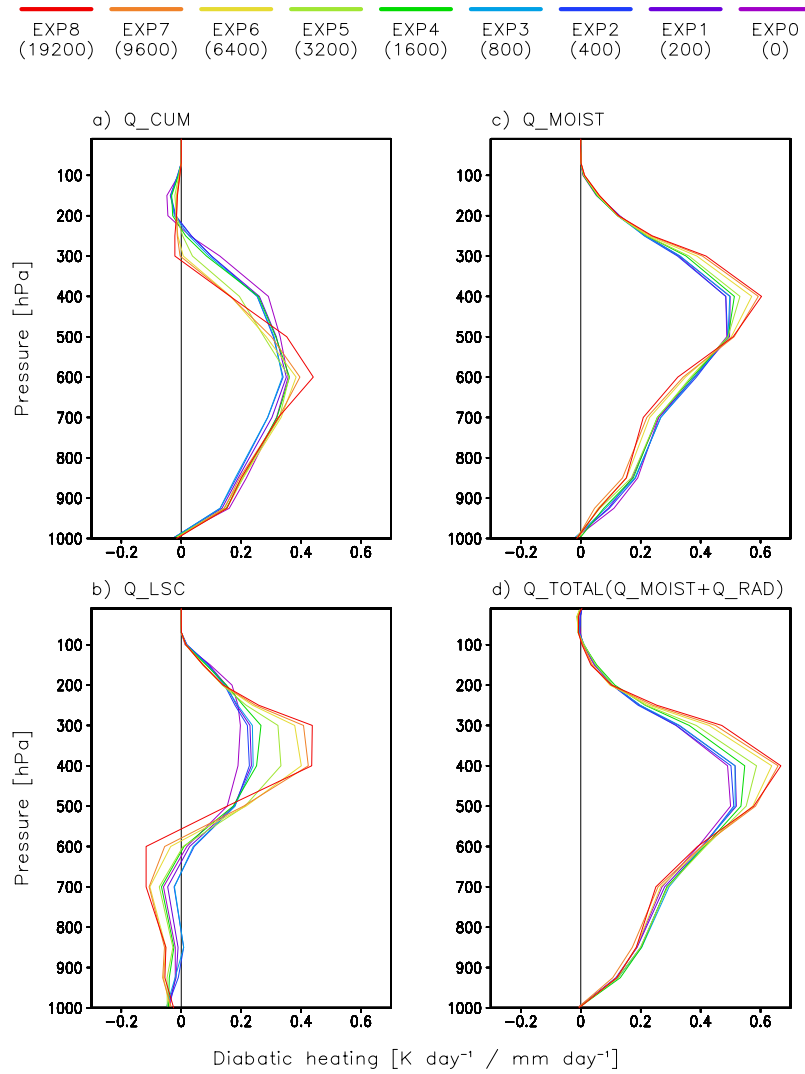


Figure 10. Same as Figure 9 but for (a) convective heating, (b) large-scale condensational heating, (c) total heating due to moist processes, and (d) total diabatic heating (moist processes plus radiation).

2001]. For dry waves the phase speed is generally determined by the dry static stability. For the moist waves, on the other hand, the phase speed is generally determined by the effective static stability [e.g., *Raymond, 2001*], with higher effective static stability generally associated with faster wave speeds. Following *Raymond [2001]* and *Lin et al. [2002]*, the effective static stability is defined as

$$\Gamma_{\text{eff}}(p) = \frac{\partial \theta}{\partial p} - \frac{\partial S_{\theta}}{\partial \omega} \quad (1)$$

where θ is the potential temperature, S_{θ} is the potential temperature source produced by the diabatic parameterizations, ω is the vertical pressure velocity, and $\partial \theta / \partial p$ is the dry static stability. The $\partial S_{\theta} / \partial \omega$ represents the effect of diabatic heating, and its value is estimated as follows: At each level we fit a straight line to a scatterplot of S_{θ} versus ω for all grid points in a specified subdomain of the numerical solution. The slope of this line is taken as the estimate of $\partial S_{\theta} / \partial \omega$.

[34] The calculated results are shown in Figure 11. The effective static stability does not change much with change in autoconversion rate (Figure 11a). This explains the nearly unchanged phase speeds of the waves with respect to different autoconversion rates (Figures 6 and 7). Actually, the dry static stability decreases significantly in the upper troposphere with increasing autoconversion rate (Figure 11b), which is caused by significant auto cooling of time-mean temperature in the upper troposphere (Figure 4a). However, the reduction of total diabatic heating associated with vertical motion (Figure 11c), which is consistent with the reduction of diabatic heating per unit precipitation (Figure 10d), almost cancels the reduction of dry static stability, leading to the nearly constant effective static stability.

[35] The changes of prominence and variance of the waves (Figures 6, 7, and 8) are more difficult to understand because (1) the variance increases with increasing autoconversion rate only for some of the waves but not others and (2) until now there is no satisfying theory on what determines the wave variances in GCMs. Most of the theoretical

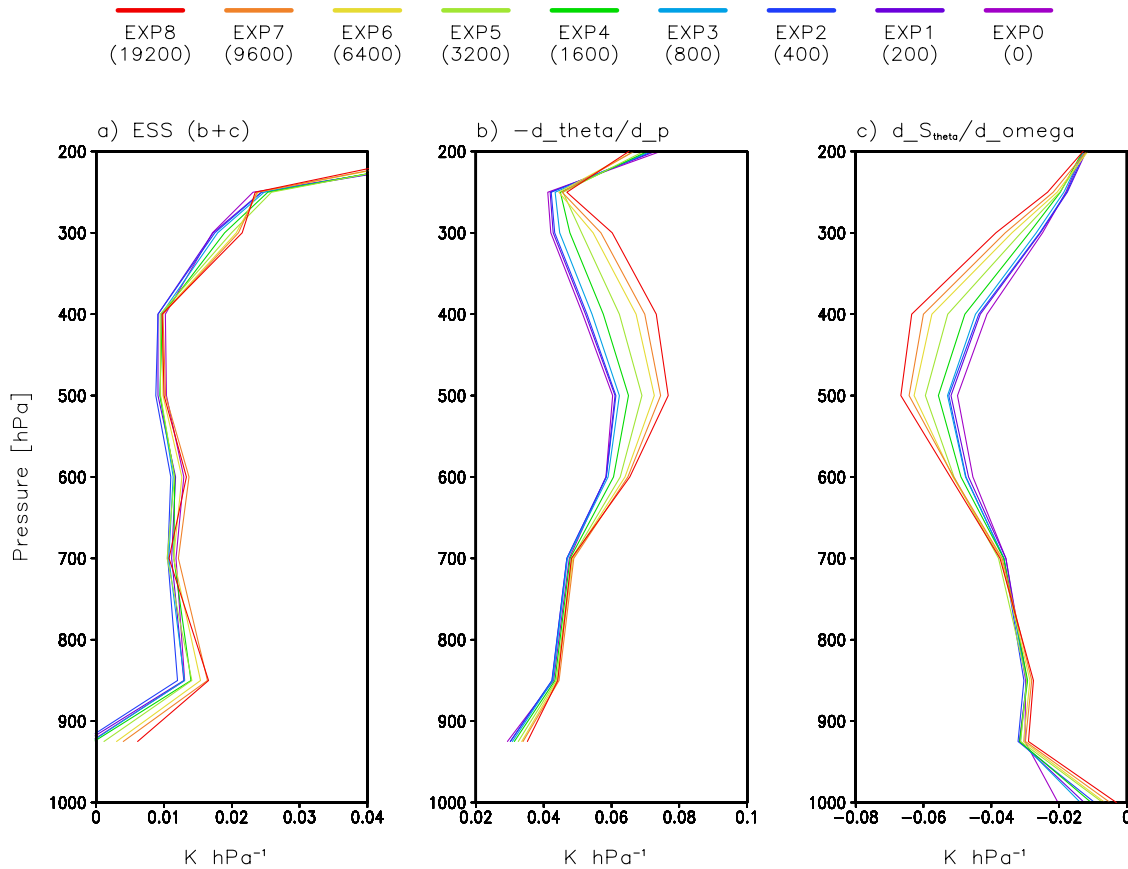


Figure 11. (a) Effective static stability, (b) dry static stability, and (c) reduction term due to diabatic heating.

studies on convectively coupled equatorial waves focus on the Kelvin wave. Therefore we plot in Figure 12 the composite life cycle of Kelvin wave in both EXP7 (control run) and EXP2. All data are area-averaged over 5°N – 5°S , 150 – 160°E . The composite life cycle is constructed using lag regression of each variable against the Kelvin wave precipitation anomaly. The lag-0 regressions of the different heating terms are similar to those shown in Figures 9 and 10, and thus will not be discussed here. We will focus on the developing stage of the Kelvin wave around lag -3 d. Increasing autoconversion rate significantly reduces the cloud amount in the upper troposphere at the developing stage (Figures 12a and 12b). This leads to an enhancement of longwave heating in the boundary layer (Figures 12c and 12d), and slight enhancement of shortwave heating in the middle troposphere (Figures 12e and 12f). The total radiative heating thus increases near the surface at the developing stage (Figures 12g and 12h). Although the heating due to moist processes does not change much in the boundary layer (Figures 12i and 12j), the total diabatic heating does increase in the boundary layer (Figures 12k and 12l), which is associated with increase of vertical motion in the boundary layer (Figures 12m and 12n) implying an enhancement of boundary layer convergence. This will enhance the frictional wave-CISK feedback mechanism and increase the wave variance [e.g., Wang and Rui, 1990].

[36] We do not find evidence for the enhancement of other feedback mechanisms in the Kelvin wave. For exam-

ple, in the free-troposphere wave-CISK mechanism [e.g., Lau and Peng, 1987], wave growth rate is determined by three factors: (1) time-mean low-level moisture with higher moisture leading to larger amplitude, (2) phase tilt of heating with height with larger tilt leading to larger amplitude, and (3) vertical heating profile with contradicting results from different studies [e.g., Lau and Peng, 1987; Chang and Lim, 1988; Cho and Pendlebury, 1997]. As shown in Figure 4b, the time-mean low-level moisture decreases with increasing autoconversion rate, which tends to suppress rather than amplify the wave variance. We do not see any significant difference between EXP2 and EXP7 in phase tilt in the free troposphere or vertical heating profile (Figures 12k and 12l). Therefore it seems that free-troposphere wave-CISK mechanism does not contribute to the enhancement of Kelvin wave variance.

[37] Figure 13 is same as Figure 12 but for the MJO. Similar to the Kelvin wave, increasing autoconversion rate also decreases cloud amount in the upper troposphere in the MJO at the developing stage around lag -10 d (Figures 13a and 13b), which leads to enhancement of longwave heating in the boundary layer (Figures 13c and 13d) and enhancement of total radiative heating in the boundary layer (Figures 13g and 13h). However, for some unknown reason, heating due to moist processes reduces in the boundary layer at the developing stage (Figures 13i and 13j), which is in contrast with the Kelvin wave (Figures 12i and 12j). This cooling cancels the warming due to radiative heating,

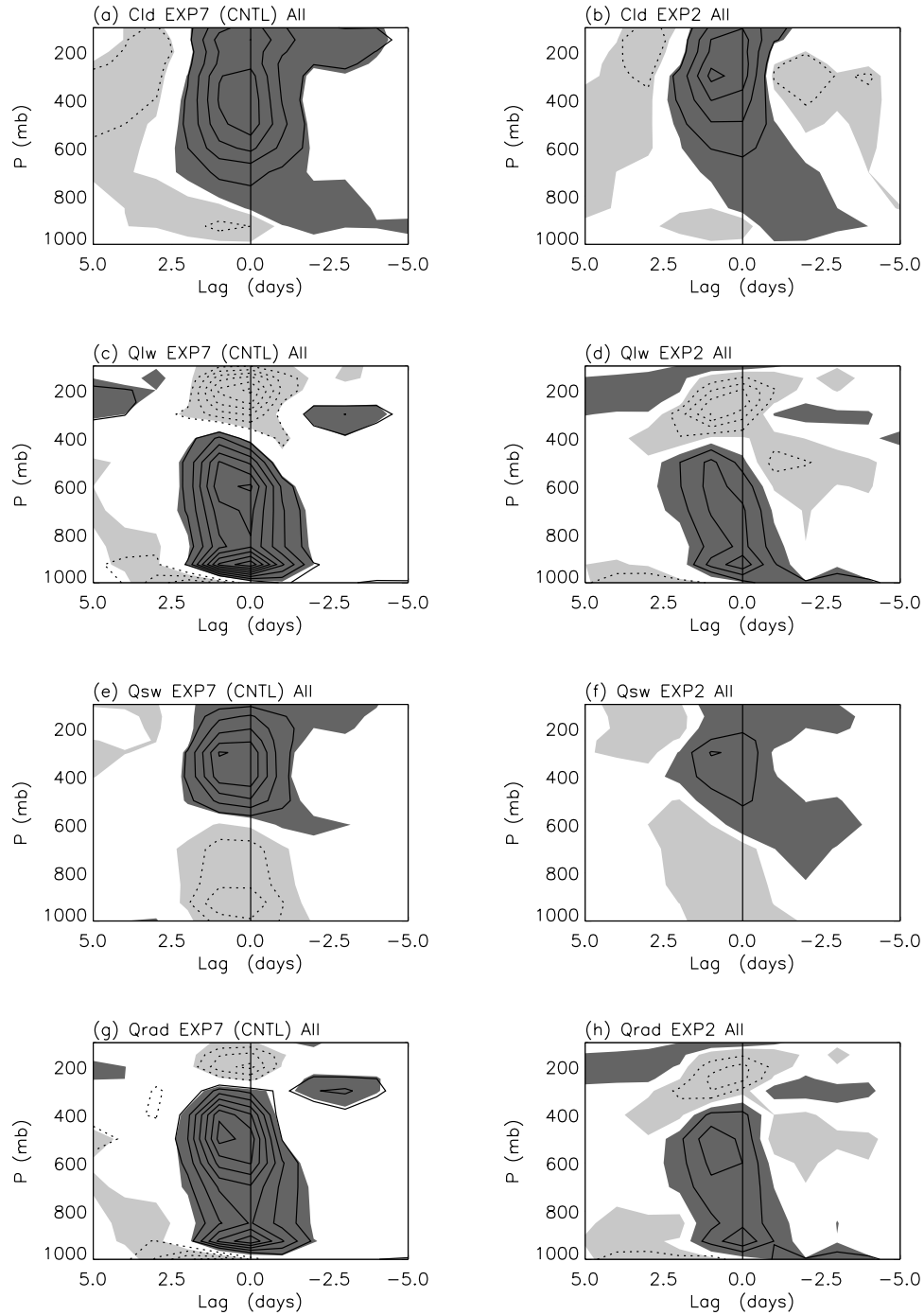


Figure 12. Lag regression against the Kelvin wave precipitation anomaly in EXP7 for (a) cloud amount ($\%/(\text{mm}/\text{d})$), (c) longwave heating rate ($(\text{W}/\text{m}^2)/(\text{mm}/\text{d})$), (e) shortwave heating rate ($(\text{W}/\text{m}^2)/(\text{mm}/\text{d})$), (g) total radiative heating rate ($(\text{W}/\text{m}^2)/(\text{mm}/\text{d})$), (i) heating due to moist processes ($(\text{W}/\text{m}^2)/(\text{mm}/\text{d})$), (k) total diabatic heating ($(\text{W}/\text{m}^2)/(\text{mm}/\text{d})$), and (m) omega ($(\text{mb}/\text{d})/(\text{mm}/\text{d})$). All data are area-averaged between 5°N – 5°S and 150 – 160°E . The corresponding structures for EXP2 are shown in (b), (d), (f), (h), (j), (l), and (n), respectively. The first contour is 5×10^{-3} , 2×10^{-2} , 2×10^{-2} , 2×10^{-2} , 1×10^{-1} , 1×10^{-1} , and 2×10^{-5} , while contour interval is 1×10^{-2} , 2×10^{-2} , 2×10^{-2} , 2×10^{-2} , 2×10^{-1} , 2×10^{-1} , and 4×10^{-5} , respectively. Shading denotes the regions where the corresponding lag correlation is above the 95% confidence level, with dark (light) shading for positive (negative) lag correlation.

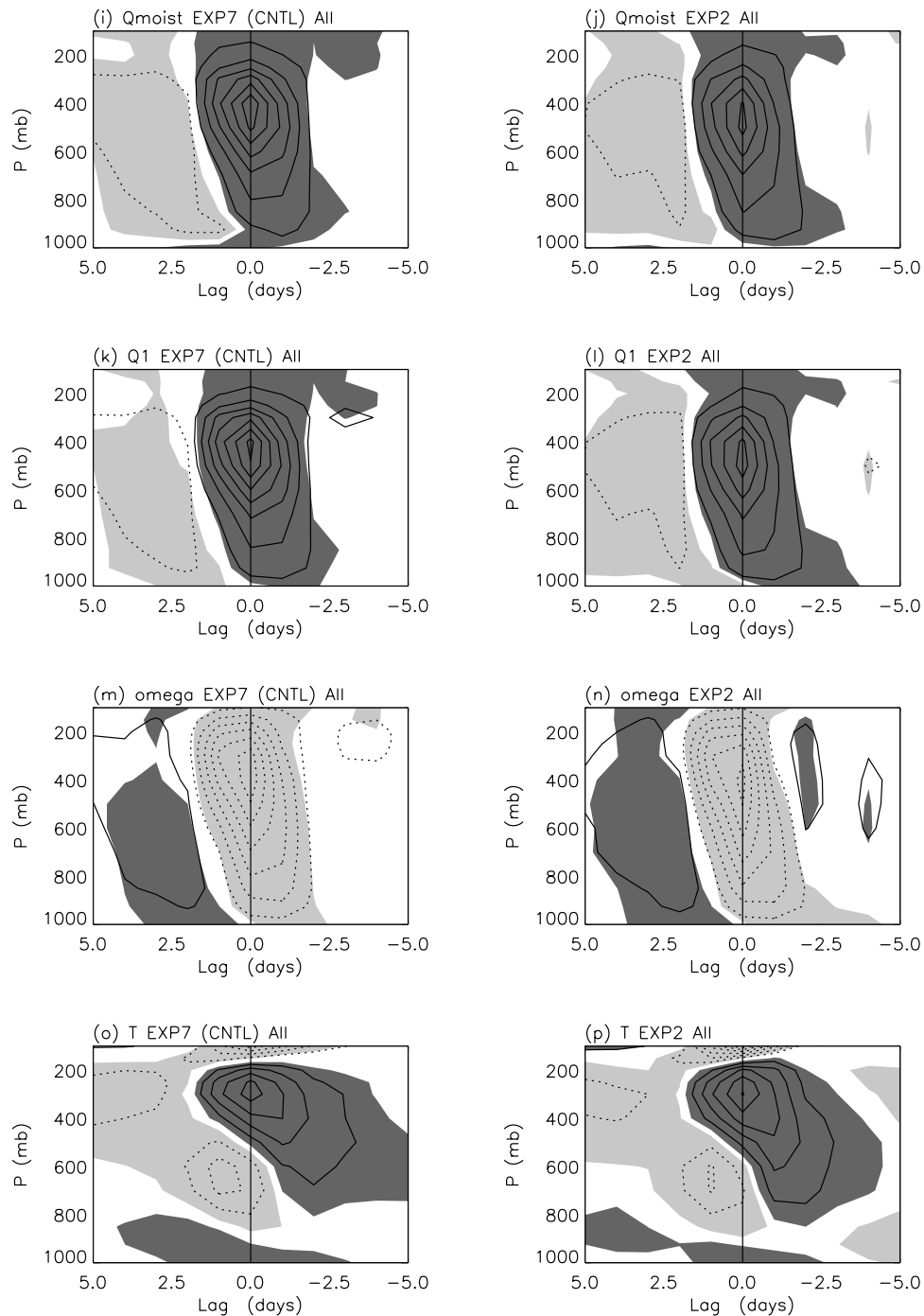


Figure 12. (continued)

making the total diabatic heating nearly unchanged in the boundary layer at the developing stage (Figures 13k and 13l). Therefore the vertical velocity and associated boundary layer convergence are nearly unchanged, and the frictional wave-CISK feedback is not enhanced. Total diabatic heatings in EXP7 and EXP2 also have similar phase tilt in the free troposphere and similar vertical heating profile (Figures 13k and 13l). The quite similar MJO heating structures in EXP7 and EXP2 may explain partly the

unchanged MJO variance associated with changing auto-conversion rate.

[38] Observations are showing the importance of life cycles of convective processes, including moisture recycling from shallow convection, deep convection and stratiform precipitation, in leading to large-scale organization of convection [e.g., *Lin et al., 2004; Mapes et al., 2006*]. The insensitivity of the MJO variance to cloud-radiative processes found here might be model dependent because of the inadequacy of representation of moisture recycling pro-

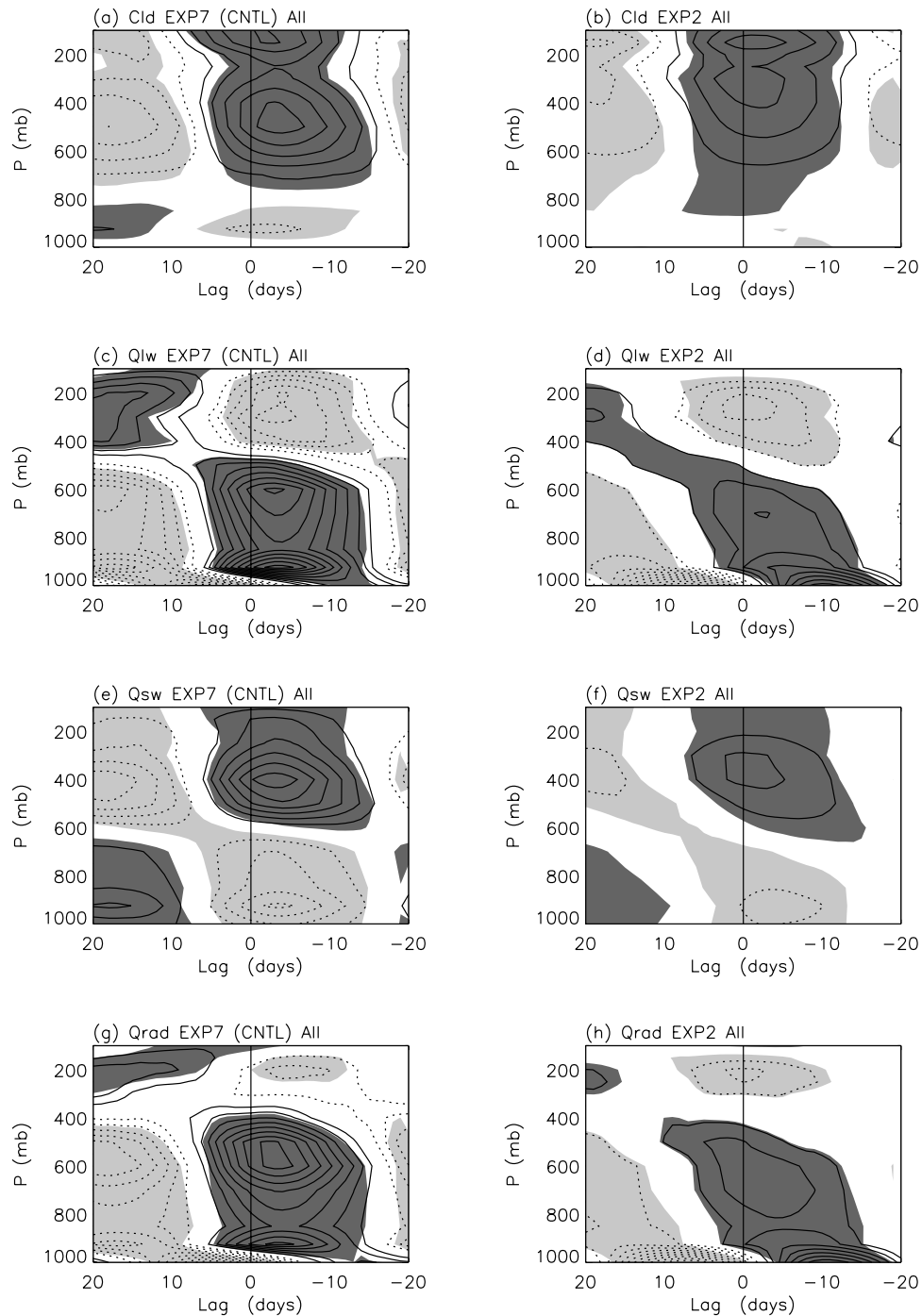


Figure 13. Same as Figure 12 but for the MJO.

cesses by shallow convection in this model as in many other GCMs. The standard setup of the RAS convection scheme used in our experiments favors the development of deep convection over shallow convection. *Lin et al.* [2007] added a moisture trigger to the RAS scheme to encourage the development of shallow/midtop convection when the lower troposphere is dry, and found that the MJO propagation is improved. Therefore it is important to parameterize well the life cycle of convective processes, especially the shallow convection in the early stage, in order to simulate well MJO. Much more analyses are

needed in future studies to understand the physical mechanisms for other waves (ER, MRG, EIG, and WIG).

5. Summary and Discussion

[39] This study examines the effects of cloud-radiative heating on convectively coupled equatorial waves simulated by the SNUGCM. The strength of cloud-radiative heating is adjusted by modifying the autoconversion rate needed for cloud condensates to grow up to raindrops. The results show that increasing the autoconversion rate has little effect

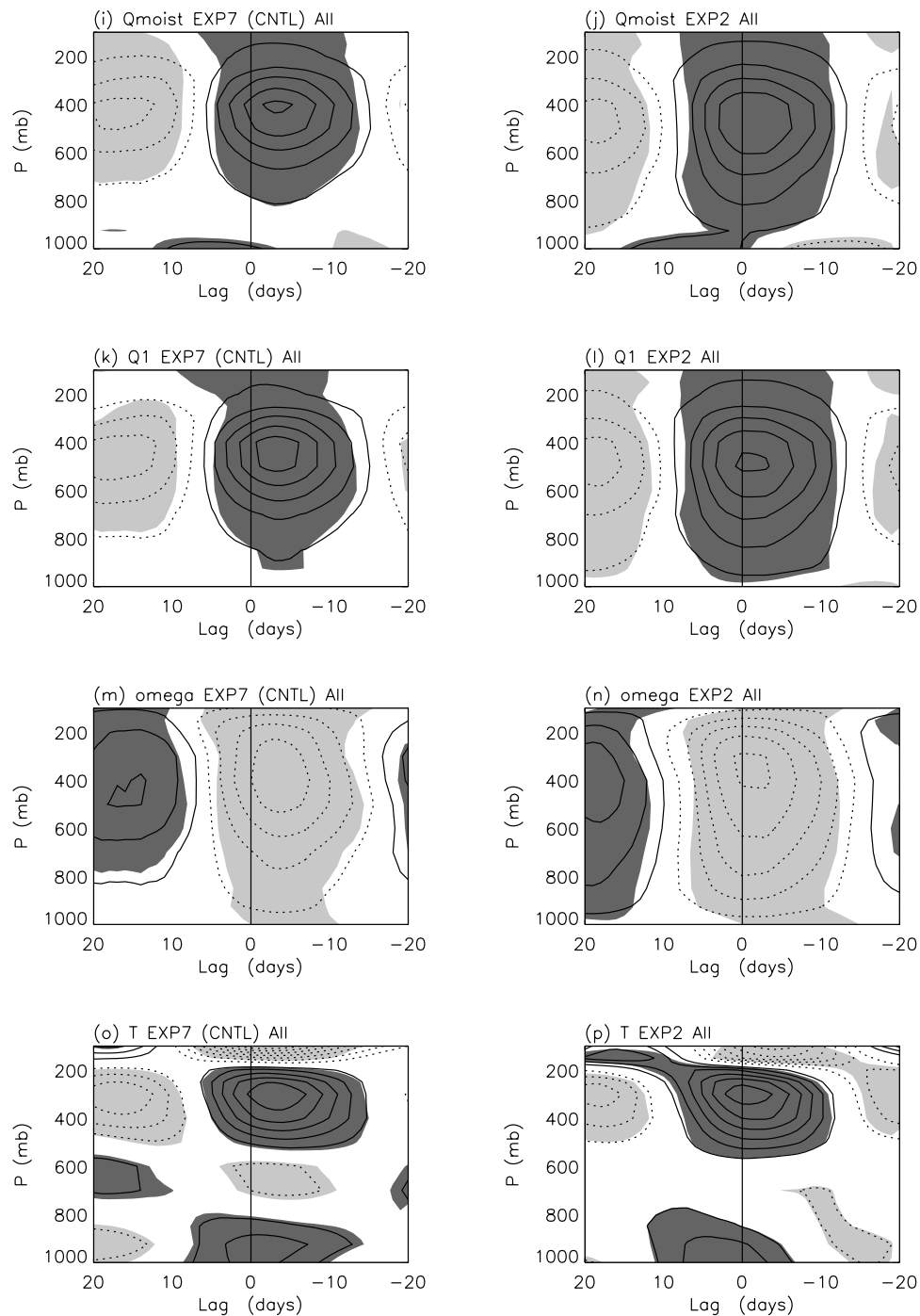


Figure 13. (continued)

on the climatological mean precipitation, but it significantly reduces the time-mean clouds and radiative heating in the upper troposphere and enhances heating due to moist processes in the middle troposphere. These lead to cooling of time-mean upper troposphere temperature and drying of lower-troposphere moisture. Reduction of cloud-radiative heating enhances the prominence of Kelvin and $n = 0$ EIG waves. It also tends to enhance significantly the variance of the Kelvin, ER, MRG, and $n = 1$ WIG waves, but not the MJO or $n = 0$ EIG wave. Reduction of cloud-radiative heating has little effect on the phase speed of the waves,

which is associated with unchanged effective static stability caused by the near cancellation between reduced dry static stability and reduced diabatic heating.

[40] The main finding of this study is that cloud-radiative heating tends to suppress AGCM-simulated convectively coupled equatorial waves. As discussed in the introduction, the cloud-radiative heating has two aspects which have opposite effect on convective heating: The column-integrated cloud-radiative heating enhances the convective heating, but the vertical profile of cloud-radiative heating tends to suppress deep convection and convective heating. Therefore

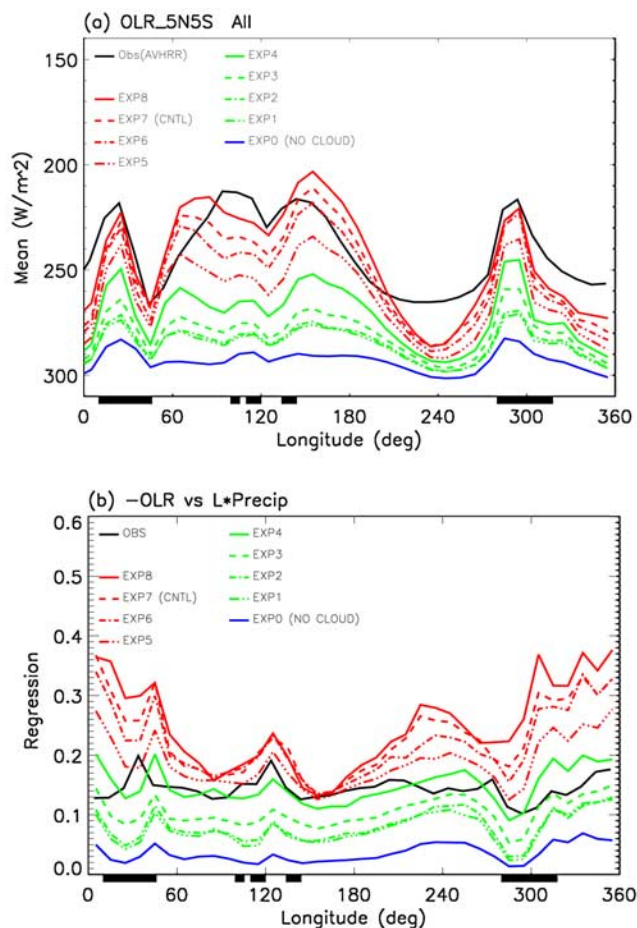


Figure 14. (a) Annual mean OLR and (b) linear regression of daily $-OLR$ versus precipitation along the equator averaged between $5^{\circ}N$ – $5^{\circ}S$ for observation and model experiments. In Figure 14b the same unit is used for both variables so that the regression coefficient is unitless.

modeling studies are needed to determine the sign of the net effect. Most of the theoretical modeling studies mainly considered the first effect, i.e., the enhancing effect of column-integrated heating [e.g., Raymond, 2001; Sobel and Gildor, 2003; Bony and Emanuel, 2005]. The GCM experiments, on the other hand, consider both the enhancing effect of column-integrated heating and the suppressing effects of vertical radiative heating profile. The radiative heating profiles in our model experiments have been analyzed by Lee *et al.* [2001] and are quite similar to those derived from observational data [e.g., Qian, 2003]. Our results show that the net effect of radiative heating is suppressing most of the convectively coupled equatorial waves, suggesting that the effect of vertical heating profile dominates over that of the column-integrated heating.

[41] Our results have important implications for improving GCM simulations of convectively coupled equatorial waves and MJO. The cloud-radiative fluxes and heating in GCMs are often tuned to match the observed TOA and surface fluxes, and our results suggest that such tuning may have strong effects on the simulated convectively coupled equatorial waves. For example, Figure 14a shows the annual

mean OLR along the equator averaged between $5^{\circ}N$ – $5^{\circ}S$ for observation and the different model experiments. The experiments that fit best the observation are EXP6, EXP7, and EXP8. However, when considering the linear regression of $-OLR$ versus precipitation (Figure 14b), which is a good estimate of the enhancement factor of cloud-radiative heating discussed in the introduction, EXP4 fits best with the observation. In other words, although EXP6, EXP7, and EXP8 simulate better time-mean TOA longwave flux, they overestimate the cloud-radiative heating at the intraseasonal timescale and thus suppress many convectively coupled equatorial waves. Therefore caution should be taken when tuning the TOA radiative fluxes, and it would be better to check simultaneously the enhancement factor of cloud-radiative heating at the intraseasonal timescale. Actually, this additional constraint may help the model to get a more realistic distribution of different cloud types [e.g., Hartmann *et al.*, 2001].

[42] **Acknowledgments.** We would like to thank the two anonymous reviewers for their insightful reviews of the manuscript. J. L. Lin is supported by the NOAA CPO/CVP program, NOAA CPO/CDEP program, and NASA MAP program. I.-S. Kang was supported by the Korea Meteorological Administration Research and Development program under grant CATER_2007-4206 and by the BK21 program.

References

- Bergman, J. W., H. H. Hendon, and K. M. Weickmann (2001), Intraseasonal air-sea interactions at the onset of El Niño, *J. Clim.*, *14*, 1702–1719.
- Bessafi, M., and M. C. Wheeler (2005), Modulation of south Indian Ocean tropical cyclones by the Madden-Julian Oscillation and convectively-coupled equatorial waves, *Mon. Weather Rev.*, *134*, 638–656.
- Bladé, I., and D. L. Hartmann (1993), Tropical intraseasonal oscillations in a simple nonlinear model, *J. Atmos. Sci.*, *50*, 2922–2939.
- Bonan, G. B. (1998), A land surface model (LSM version 1.0) for ecological, hydrological, and atmospheric studies: Technical description and user's guide, *NCAR/TN-417+STR*, 150 pp., Natl. Cent. for Atmos. Res., Boulder, Colo.
- Bony, S., and K. A. Emanuel (2005), On the role of moist processes in tropical intraseasonal variability: Cloud-radiation and moisture-convection feedbacks, *J. Atmos. Sci.*, *62*, 2770–2789.
- Bretherton, C. S., and A. H. Sobel (2002), A simple model of a convectively coupled Walker circulation using the weak temperature gradient approximation, *J. Clim.*, *15*, 2907–2920.
- Chang, C. P., and H. Lim (1988), Kelvin wave-CISK: A possible mechanism for the 30–50 day oscillations, *J. Atmos. Sci.*, *45*, 1709–1720.
- Cho, H.-R., and D. Pendlebury (1997), Wave CISK of equatorial waves and the vertical distribution of cumulus heating, *J. Atmos. Sci.*, *54*, 2429–2440.
- Emanuel, K. A. (1987), An air-sea interaction model of intraseasonal oscillation in the tropics, *J. Atmos. Sci.*, *44*, 2324–2340.
- Hartmann, D. L., L. A. Moy, and Q. Fu (2001), Tropical convection and the energy balance at the top of the atmosphere, *J. Clim.*, *14*, 4495–4511.
- Hayashi, Y., and D. G. Golder (1986), Tropical intraseasonal oscillations appearing in a GFDL general circulation model and FGGE data. part I: Phase propagation, *J. Atmos. Sci.*, *43*, 3058–3067.
- Hayashi, Y., and D. G. Golder (1988), Tropical intraseasonal oscillations appearing in a GFDL general circulation model and FGGE data. part II: Structure, *J. Atmos. Sci.*, *45*, 3017–3033.
- Hayashi, Y., and D. G. Golder (1997), United mechanisms for the generation of low- and high-frequency tropical waves. part I: Control experiments with moist convective adjustment, *J. Atmos. Sci.*, *54*, 1262–1276.
- Hayashi, Y., and A. Sumi (1986), The 30–40 day oscillation simulated in an “aqua planet” model, *J. Meteorol. Soc. Jpn.*, *64*, 451–466.
- Hendon, H. H., C. Zhang, and J. D. Glick (1999), Interannual variation of the MJO during austral summer, *J. Clim.*, *12*, 2538–2550.
- Holtlag, A. A. M., and B. A. Boville (1993), Local versus non-local boundary layer diffusion in a global climate model, *J. Clim.*, *6*, 1825–1842.
- Huffman, G. J., R. F. Adler, M. M. Morrissey, S. Curtis, R. Joyce, B. McGavock, and J. Susskind (2001), Global precipitation at one-degree daily resolution from multi-satellite observations, *J. Hydrometeorol.*, *2*, 36–50.

- Janowiak, J. E., and P. A. Arkin (1991), Rainfall variations in the tropics during 1986–1989, as estimated from observations of cloud-top temperatures, *J. Geophys. Res.*, **96**, 3359–3373.
- Kessler, W. S., M. J. McPhaden, and K. M. Weickmann (1995), Forcing of intraseasonal Kelvin waves in the equatorial Pacific, *J. Geophys. Res.*, **100**, 10,613–10,631.
- Lau, K. M., and L. Peng (1987), Origin of low-frequency (intraseasonal) oscillations in the tropical atmosphere, *J. Atmos. Sci.*, **44**, 950–972.
- Lau, K. M., H. T. Wu, Y. C. Sud, and G. K. Walker (2005), Effects of cloud microphysics on tropical atmospheric hydrologic processes and intraseasonal variability, *J. Clim.*, **18**, 4731–4751.
- Lau, N. C., I. M. Held, and J. D. Neelin (1988), The Madden-Julian Oscillations in an idealized general circulation model, *J. Atmos. Sci.*, **45**, 3810–3831.
- Lee, M.-I., I.-S. Kang, J.-K. Kim, and B. E. Mapes (2001), Influence of cloud-radiation interaction on simulating tropical intraseasonal oscillation with an atmospheric general circulation model, *J. Geophys. Res.*, **106**, 14,219–14,233.
- Lee, M.-I., I.-S. Kang, and B. E. Mapes (2003), Impacts of cumulus convection parameterization on aqua-planet AGCM simulations of tropical intraseasonal variability, *J. Meteorol. Soc. Jpn.*, **81**, 963–992.
- Le Treut, H., and Z.-X. Li (1991), Sensitivity of an atmospheric general circulation model to prescribed SST changes: Feedback effects associated with the simulation of cloud optical properties, *Clim. Dyn.*, **5**, 175–187.
- Liebmann, B., H. H. Hendon, and J. D. Glick (1994), The relationship between tropical cyclones of the western Pacific and Indian Oceans and the Madden-Julian Oscillation, *J. Meteorol. Soc. Jpn.*, **72**, 401–411.
- Lin, J. L., and B. E. Mapes (2004), Radiation budget of the tropical intraseasonal oscillation, *J. Atmos. Sci.*, **61**, 2050–2062.
- Lin, J. L., M. H. Zhang, and B. E. Mapes (2002), Does the tropical atmosphere support large-scale radiative-convective overturning?, paper presented at the 25th Conference on Hurricanes and Tropical Meteorology, abstract 15B.2a, pp. 589–590, Am. Meteorol. Soc., San Diego, Calif.
- Lin, J. L., B. E. Mapes, M. H. Zhang, and M. Newman (2004), Stratiform precipitation, vertical heating profiles, and the Madden-Julian Oscillation, *J. Atmos. Sci.*, **61**, 296–309.
- Lin, J. L., et al. (2006), Tropical intraseasonal variability in 14 IPCC AR4 climate models. part I: Convective signals, *J. Clim.*, **19**, 2665–2690.
- Lin, J. L., M.-I. Lee, D. Kim, I.-S. Kang, and D. Frierson (2007), The impacts of convective parameterization and moisture triggering on AGCM-simulated convectively coupled equatorial waves, *J. Clim.*, in press.
- Madden, R. A., and P. R. Julian (1971), Detection of a 40–50 day oscillation in the zonal wind in the tropical Pacific, *J. Atmos. Sci.*, **28**, 702–708.
- Majda, A. J., and R. Klein (2003), Systematic multiscale models for the tropics, *J. Atmos. Sci.*, **60**, 393–408.
- Maloney, E. D., and D. L. Hartmann (2001), The Madden-Julian Oscillation, barotropic dynamics, and north Pacific tropical cyclone formation. part I: Observations, *J. Atmos. Sci.*, **58**, 2545–2558.
- Mapes, B. E., S. Tulich, J. L. Lin, and P. Zuidema (2006), Mesoscale convection life cycle: Building block or prototype for large-scale tropical waves?, *Dyn. Atmos. Oceans*, **42**, 3–29.
- Matsuno, T. (1966), Quasi-geostrophic motions in the equatorial area, *J. Meteorol. Soc. Jpn.*, **44**, 25–43.
- Nakajima, T., M. Tsukamoto, Y. Tsumahima, and A. Numaguti (1995), Modelling of the radiative processes in an AGCM, in *Climate System Dynamics and Modelling*, vol. 1–3, edited by T. Matsuno, pp. 104–123, Univ. of Tokyo, Tokyo.
- Neelin, J. D., I. M. Held, and K. H. Cook (1987), Evaporation-wind feedback and low-frequency variability in the tropical atmosphere, *J. Atmos. Sci.*, **44**, 2341–2348.
- Numaguti, A., M. Takahashi, T. Nakajima, and A. Sumi (1995), Development of an atmospheric general circulation model, in *Climate System Dynamics and Modelling*, vol. 1–3, edited by T. Matsuno, pp. 1–27, Univ. of Tokyo, Tokyo.
- Qian, T. (2003), Cloud vertical structure and radiative heating profiles during TOGA COARE, Ph.D. thesis, 141 pp., State Univ. of New York at Stony Brook, Stony Brook, N. Y.
- Raymond, D. J. (2001), A new model of the Madden–Julian Oscillation, *J. Atmos. Sci.*, **58**, 2807–2819.
- Roundy, P. E., and G. N. Kiladis (2006), Observed relationships between intraseasonal oceanic Kelvin waves and atmospheric forcing, *J. Clim.*, **19**, 5253–5272.
- Salby, M., and R. R. Garcia (1987), Transient response to localized episodic heating in the tropics. part I: Excitation and short-time near-field behavior, *J. Atmos. Sci.*, **44**, 458–498.
- Salby, M. L., and H. H. Hendon (1994), Intraseasonal behavior of clouds, temperature, and motion in the tropics, *J. Atmos. Sci.*, **51**, 2207–2224.
- Slingo, J. M., and R. A. Madden (1991), Characteristics of the tropical intraseasonal oscillation in the NCAR community climate model, *Q. J. R. Meteorol. Soc.*, **117**, 1129–1169.
- Slingo, J. M., et al. (1996), Intraseasonal oscillations in 15 atmospheric general circulation models: Results from an AMIP diagnostic subproject, *Clim. Dyn.*, **12**, 325–357.
- Sobel, A. H., and C. S. Bretherton (2000), Modeling tropical precipitation in a single column, *J. Clim.*, **13**, 4378–4392.
- Sobel, A. H., and H. Gildor (2003), A simple time-dependent model of SST hot spots, *J. Clim.*, **16**, 3978–3992.
- Takayabu, Y. N. (1994), Large-scale cloud disturbances associated with equatorial waves. part I: Spectral features of the cloud disturbances, *J. Meteorol. Soc. Jpn.*, **72**, 433–448.
- Takayabu, Y. N., T. Iguchi, M. Kachi, A. Shibata, and H. Kanzawa (1999), Abrupt termination of the 1997–98 El Niño in response to a Madden-Julian Oscillation, *Nature*, **402**, 279–282.
- Tiedtke, M. (1983), The sensitivity of the time-mean large-scale flow to cumulus convection in the ECMWF model, in *Proceedings of the ECMWF Workshop on Convection in Large-Scale Models*, pp. 297–316, Eur. Cent. for Medium-Range Weather Forecasts, Reading, England, 28 November to 1 December.
- Waliser, D., S. Schubert, A. Kumar, K. Weickmann, and R. Dole (2003), Proceedings from a workshop on Modeling, Simulation and Forecasting of Subseasonal Variability, *NASA/CP 2003-104606*, vol. 25, pp. 62, Natl. Aeronaut. and Space Admin., Greenbelt, Md.
- Wang, B., and H. Rui (1990), Dynamics of the coupled moist Kelvin–Rossby wave on an equatorial β -plane, *J. Atmos. Sci.*, **47**, 398–413.
- Wheeler, M., and G. N. Kiladis (1999), Convectively coupled Equatorial waves: Analysis of clouds and temperature in the wave number-frequency domain, *J. Atmos. Sci.*, **56**, 374–399.
- Wheeler, M., G. N. Kiladis, and P. J. Webster (2000), Large-scale dynamical fields associated with convectively coupled equatorial waves, *J. Atmos. Sci.*, **57**, 613–640.
- Wheeler, M. C., and J. L. McBride (2005), Australian-Indonesian monsoon, in *Intraseasonal Variability in the Atmosphere–Ocean Climate System*, edited by W. K. M. Lau and D. E. Waliser, pp. 125–173, Springer, New York.
- Yasunari, T. (1979), Cloudiness fluctuations associated with the northern hemisphere summer monsoon, *J. Meteorol. Soc. Jpn.*, **57**, 227–242.
- Yuter, S. E., and R. A. Houze Jr. (2000), The 1997 Pan American Climate Studies Tropical Eastern Pacific Process Study. part I: ITCZ Region, *Bull. Am. Meteorol. Soc.*, **81**, 451–481.

I.-S. Kang and D. Kim, Department of Atmospheric Sciences, Seoul National University, Seoul 151-742, Korea.

M.-I. Lee, Global Modeling and Assimilation Office, Code 610.1, Goddard Space Flight Center, Greenbelt, MD 20771, USA.

J.-L. Lin, Department of Geography, Ohio State University, 1105 Derby Hall, 154 North Oval Mall, Columbus, OH 43210, USA. (lin.789@osu.edu)